

## THE SLOAN LENS ACS SURVEY. V. THE FULL ACS STRONG-LENS SAMPLE<sup>1</sup>

ADAM S. BOLTON<sup>2,3</sup>, SCOTT BURLES<sup>4</sup>, LÉON V. E. KOOPMANS<sup>5</sup>, TOMMASO TREU<sup>6,7</sup>, RAPHAËL GAVAZZI<sup>6,8</sup>,  
LEONIDAS A. MOUSTAKAS<sup>9</sup>, RANDALL WAYTH<sup>3</sup>, AND DAVID J. SCHLEGEL<sup>10</sup>

*Accepted for publication in The Astrophysical Journal*

### ABSTRACT

We present the definitive data for the full sample of 131 strong gravitational lens candidates observed with the Advanced Camera for Surveys (ACS) aboard the *Hubble Space Telescope* by the Sloan Lens ACS (SLACS) Survey. All targets were selected for higher-redshift emission lines and lower-redshift continuum in a single Sloan Digital Sky Survey (SDSS) spectrum. The foreground galaxies are primarily of early-type morphology, with redshifts from  $z \simeq 0.05$  to 0.5 and velocity dispersions from  $\sigma \simeq 160 \text{ km s}^{-1}$  to  $400 \text{ km s}^{-1}$ ; the faint background emission-line galaxies have redshifts ranging from  $z \simeq 0.2$  to 1.2. We confirm 70 systems showing clear evidence of multiple imaging of the background galaxy by the foreground galaxy, as well as an additional 19 systems with probable multiple imaging. For 63 clear lensing systems, we present singular isothermal ellipsoid and light-traces-mass gravitational lens models fitted to the ACS imaging data. These strong-lensing mass measurements are supplemented by magnitudes and effective radii measured from ACS surface-brightness photometry and redshifts and velocity dispersions measured from SDSS spectroscopy. These data constitute a unique resource for the quantitative study of the inter-relations between mass, light, and kinematics in massive early-type galaxies. We show that the SLACS lens sample is statistically consistent with being drawn at random from a parent sample of SDSS galaxies with comparable spectroscopic parameters and effective radii, suggesting that the results of SLACS analyses can be generalized to the massive early-type population.

*Subject headings:* gravitational lensing — galaxies: elliptical — surveys

### 1. INTRODUCTION

Strong gravitational lensing—the multiple imaging of a distant object by the gravity of an intervening object—provides a direct and accurate measurement of mass in the central regions of elliptical galaxies. This measurement is independent of the dynamical state of the lensing material and nearly independent of its radial density profile (e.g. Kochanek 1991). Until recently, strong lenses were relatively rare and heterogeneously selected, a fact which has imposed serious limitations on

their utility for statistically significant scientific studies. Systematic surveys employing various observational techniques have been conducted in an attempt to surmount this limitation. In the radio domain, significant contributions to the number of known galaxy-scale lenses have been made by the survey of Winn et al. (2000, 2001, 2002a,b) based on the Parkes-MIT-NRAO catalog (Griffith & Wright 1993) and by the Cosmic Lens All-Sky Survey (CLASS: Myers et al. 2003; Browne et al. 2003). Miralda-Escude & Lehar (1992) predicted that large numbers of strong galaxy-galaxy lenses should be visible at optical wavelengths. Many such systems have now been discovered through spectroscopic selection of candidate objects from within the Sloan Digital Sky Survey (SDSS; York et al. 2000) database by the Sloan Lens ACS Survey (SLACS: Bolton et al. 2006; Treu et al. 2006; Koopmans et al. 2006; Gavazzi et al. 2007, 2008; Bolton et al. 2008, hereafter Papers I–IV and VI–VII respectively; also see Bolton et al. 2005 and Bolton et al. 2007, hereafter B07) and the Optimal Line-of-Sight Survey (OLS; Willis et al. 2005, 2006). Numerous strong galaxy-galaxy lenses and lens candidates have also been identified through various combinations of visual and automated inspection of large-area imaging surveys (Ratnatunga et al. 1999; Fassnacht et al. 2004; Moustakas et al. 2007; Cabanac et al. 2007; Belokurov et al. 2007; Kubo & Dell’Antonio 2008; Faure et al. 2008). Finally, significant numbers of lensed quasars have been detected through *Hubble Space Telescope* Snapshot observations of known quasars (Maoz et al. 1993; Morgan et al. 2003), by high-resolution ground-based surveys of the Hamburg-ESO bright quasar catalog (Wisotzki et al. 1993, 1996, 1999; Gregg et al. 2000; Wisotzki et al. 2002, 2004;

<sup>1</sup> Based on observations made with the NASA/ESA *Hubble Space Telescope*, obtained at the Space Telescope Science Institute, which is operated by AURA, Inc., under NASA contract NAS 5-26555. These observations are associated with programs #10174, #10494, #10587, #10798, and #10886.

<sup>2</sup> Beatrice Watson Parrent Fellow, Institute for Astronomy, University of Hawai‘i, 2680 Woodlawn Dr., Honolulu, HI 96822 (bolton@ifa.hawaii.edu)

<sup>3</sup> Harvard-Smithsonian Center for Astrophysics, 60 Garden St., Cambridge, MA 02138 (rwayth@cfa.harvard.edu)

<sup>4</sup> Department of Physics and Kavli Institute for Astrophysics and Space Research, Massachusetts Institute of Technology, 77 Massachusetts Avenue, Cambridge, MA 02139 (burles@mit.edu)

<sup>5</sup> Kapteyn Astronomical Institute, University of Groningen, P.O. Box 800, 9700AV Groningen, The Netherlands (koopmans@astro.rug.nl)

<sup>6</sup> Department of Physics, University of California, Santa Barbara, CA 93101, USA (tt@physics.ucsb.edu)

<sup>7</sup> Sloan Fellow, Packard Fellow

<sup>8</sup> Institut d’Astrophysique de Paris, UMR7095 CNRS & Univ. Pierre et Marie Curie, 98bis Bvd Arago, F-75014 Paris, France (gavazzi@iap.fr)

<sup>9</sup> Jet Propulsion Laboratory, California Institute of Technology, 4800 Oak Grove Drive, M/S 169-327, Pasadena, CA 91109 (leonidas@jpl.nasa.gov)

<sup>10</sup> Physics Division, Lawrence Berkeley National Laboratory, Berkeley, CA 94720-8160, USA (djschlegel@lbl.gov)

Blackburne et al. 2008), and by the SDSS Quasar Lens Search within the SDSS imaging database (Oguri et al. 2006; Inada et al. 2007; Oguri et al. 2007). To these systematic discoveries one must also add the many serendipitously discovered strong lenses that comprise a large fraction of the known lens population.

Here we report the observational results of the SLACS Survey from its initiation through the deactivation of the *HST* Advanced Camera for Surveys (ACS) in 2007 January. From among 131 successfully observed candidates, we confirm a total of 70 secure strong gravitational lenses and a further 19 possible gravitational lenses, making the SLACS Survey the most productive strong-lens survey to date. As a consequence of the spectroscopic selection method, all of the SLACS lenses have known spectroscopic redshifts for both foreground and background galaxies, giving the SLACS sample an immediate quantitative scientific advantage over strong-lens candidate samples selected from imaging data. This paper represents the definitive source for SLACS Survey data, pending the publication of multi-color *HST* photometry (primarily from the WFPC2 instrument) currently being completed during Observing Cycle 16, and of a modest number of additional lenses confirmed with WFPC2 imaging during Cycle 15. The organization of this work is as follows. In §2 we describe the candidate selection and *HST* observing strategy. Section 3 presents our data-reduction procedures. Section 4 describes the photometric modeling methods that we apply to the images of the foreground galaxies. We employ both elliptical radial B-spline models (to obtain detailed light profiles and to generate residual images for strong lens modeling) and elliptical de Vaucouleurs (1948) models (to measure global magnitudes and structural parameters). The details of our strong gravitational lens analysis are presented in §5. Our lens classification procedure and an overview of the resulting lens sample is presented in §5.1. Section 5.2 describes our strong-lens mass modeling procedure as applied to 63 of the secure strong lens systems, yielding the aperture-mass measurements that enable the scientific applications of the sample. In §6 we compare our measurements with quantities obtained through other methods, as a cross check and in order to make realistic estimates of our measurement errors. Section 7 examines the representativeness of the SLACS lenses among early-type galaxies in general. We summarize and offer some concluding remarks in §8. Appendix A provides complete data tables and image figures, as well as comments on the 7 secure lenses that do not admit simple lens-modeling analysis.

Throughout this work, we assume a general-relativistic Friedmann-Robertson-Walker (FRW) cosmology with matter-density parameter  $\Omega_M = 0.3$ , vacuum energy-density parameter  $\Omega_\Lambda = 0.7$ , and Hubble parameter  $H_0 = 70 \text{ km s}^{-1} \text{ Mpc}^{-1}$ . Magnitudes are quoted in the AB system.

## 2. SAMPLE SELECTION AND OBSERVATIONS

The gravitational lenses presented in this work were all selected from the spectroscopic database of the SDSS based on the presence of absorption-dominated galaxy continuum at one redshift and nebular emission lines (Balmer series, [OII] 3727, or [OIII] 5007) at another, higher redshift. The spectroscopic lens survey tech-

nique was first envisioned by Warren et al. (1996) and Hewett et al. (2000) following the serendipitous discovery of the gravitational lens 0047–2808 through the presence of high-redshift Lyman- $\alpha$  emission in the spectrum of the targeted lower redshift elliptical galaxy. Further details of our particular approach are provided in Bolton et al. (2004) and Paper I. The SLACS Survey includes candidates from the SDSS MAIN galaxy sample (Strauss et al. 2002) in addition to candidates from the SDSS luminous red galaxy (LRG) sample (Eisenstein et al. 2001). Most candidates were selected on the basis of multiple emission lines, though several lens candidates were observed under *HST* program #10886 on the basis of secure [OII] 3727 line detections alone. By virtue of this spectroscopic selection method, all SLACS lenses and lens candidates have secure foreground (“lens”) and background (“source”) redshifts from the outset. Accurate redshifts such as these are essential to all quantitative scientific applications of strong lensing.

From among the set of spectroscopically identified candidates, target lists for follow-up *HST* imaging observations were created based on a number of competing considerations: (1) maximal nominal lensing cross sections, as determined from foreground and background redshifts and SDSS velocity dispersions using a singular isothermal sphere model; (2) a reasonably uniform distribution in lens redshifts and velocity dispersions, within the limits of feasibility; and (3) the significance of the spectroscopic detection of background emission lines.

The selected candidates were observed under three discovery programs: #10174 (Cycle 13, PI: L. Koopmans), #10587 (Cycle 14, PI: A. Bolton), and #10886 (Cycle 15, PI: A. Bolton). Program #10174 was executed as a Snapshot program, with two 420-s exposures per visit: one through the F435W filter and one through the F814W filter. Program #10587 was originally implemented identically to #10174, but the F435W exposures were canceled early in the observing cycle, since the advent of 2-gyro *HST* guiding had significantly reduced Snapshot program execution rates relative to previous cycles. This reduction in Snapshot execution rates somewhat compromised the specific goal of program #10587 to obtain a greater number of lower-mass gravitational lens galaxies, which have a lower confirmation rate by virtue of their smaller lensing cross section. Nevertheless, as seen in B07 and Paper VII, the resulting combined SLACS lens sample has sufficient leverage in mass to define mass-dynamical and mass-luminosity scaling relations for the luminous early-type galaxy population. Program #10886 was executed as a General Observer (GO) program, with one orbit per target through the F814W filter, split among four closely dithered pointings. New lenses confirmed by these discovery programs were subsequently scheduled for observation with full orbits and through complementary filters under programs #10494, #10798, and #11202 (Cycles 14, 15, and 16, respectively; PI: L. Koopmans). All programs used the Wide-Field Channel (WFC) of the ACS until the untimely demise of that camera in 2007 January prompted a transfer of the program to WFPC2.

The work presented here is based on the full SLACS *HST*-ACS dataset, and includes data from all SLACS programs except #11202, which is carried out entirely

with the WFPC2. The analysis in the current paper makes exclusive use of the F814W (*I*-band) data, since all ACS targets were observed at least once through this filter. Multi-color coverage of the SLACS lens sample is currently being obtained under program #11202; multi-band results based on ACS, WFPC2, and NICMOS data will be published following the completion of *HST* Observing Cycle 16.

### 3. DATA REDUCTION

All ACS frames were downloaded from the online archive at the Space Telescope Science Institute on 2007 April 03, having been processed by version 4.6.1 of the CALACS calibration software. The following steps were applied to all frames, after the generation of a catalog file associating multiple exposure, filters, and visits to the same unique target with one another:

1. From the “FLT” file, extract the central  $1500 \times 1500$  pixel (roughly  $75'' \times 75''$ ) section of the ACS WF1 aperture, in which the targets were centered.
2. Subtract the sky level as determined by the MULTIDRIZZLE software and recorded in the MDRIZSKY header parameter.
3. Identify and mask significantly negative “cold pixels” in the cutout, then process the cutout with the L.A. Cosmic software (van Dokkum 2001, as implemented in IDL) in order to identify and mask cosmic rays (CRs).
4. Tabulate manually the approximate pixel location of the target galaxy in each exposure. For multi-exposure visits, obtain the approximate shift between exposures through image cross correlation.
5. Use the distortion information in the fits headers to generate tangent-plane RA and Dec coordinate images relative to a fixed reference pixel.
6. Find the centroid of the target galaxy in each frame by fitting an elliptical Moffat profile as a function of RA and Dec (without point-spread function convolution) to the image using the MPFIT2DPEAK non-linear fitting routine in IDL.
7. Rectify the individual frames onto a uniform  $0.05''$  grid (centered on the RA and Dec centroid from the previous step) via bilinear interpolation within the images as dictated by the distortion solution. Also rectify, with identical sampling, an appropriate model point-spread function (PSF) as determined by the Tiny Tim software (Krist 1993) using an input spectral energy distribution equal to the median of all normalized SDSS spectra of SLACS targets.
8. Divide the counts and count-errors of each frame by the exposure time to convert to counts per second.
9. For sets of multiple dithered exposures, combine all exposures into a single stacked exposure, with an additional CR-rejection step. Similarly, combine the PSF samplings corresponding to the individual exposures.

10. Visually classify all targets for multiplicity and morphology. Systems with two or more foreground galaxies of comparable luminosity are classified as “multiple”, while systems with only a single dominant foreground galaxy are classified as “single”. Morphological classification is made by a consensus of the authors through the inspection of F814W ACS data alone, and is limited to the categories of “early-type” (elliptical and S0), “late-type” (Sa and later spirals), and “unclassified” (generally ambiguous between S0 and Sa).

We adopt this recipe in preference to the MULTIDRIZZLE reduction package because the “drizzle” re-sampling algorithm (Fruchter & Hook 2002) is not well suited to single-exposure Snapshot data. By using the above reduction procedure for both Snapshot and dithered multi-exposure imaging data, we guarantee that our analysis is as uniform as possible.

### 4. PHOTOMETRIC MEASUREMENT

This section describes the details of our ACS F814W surface photometry. This photometric modeling pertains exclusively to the bright, foreground galaxy in each candidate lens system: i.e., the “lens” in the case of a bona fide strong lens system. These photometric models serve to characterize the brightnesses, sizes, and shapes of the foreground galaxies, as well as to generate model-subtracted residual images of the background galaxies suitable for the strong-lensing classification and modeling described in §5.2. Depending upon the particular application, we use either radial B-spline models or de Vaucouleurs (1948) models. Direct F814W images of all ACS targets are shown in Figure 5 (in Appendix A).

#### 4.1. Radial B-spline analysis

SLACS provides a sample of bright lensing galaxies with relatively faint lensed galaxies in the background. While this is a benefit to the study of the lens galaxies themselves, it presents a challenge for strong-lens mass models that must be fitted to those faint lensed features. We address this challenge with the radial B-spline galaxy image modeling technique, introduced in Paper I. Radial B-splines provide a generalized basis for modeling the radial luminosity profile of early-type galaxies, including low-order angular effects through the inclusion of multipole terms. By virtue of their significant freedom, the radial B-spline models are able to produce very cleanly subtracted residual images of the (often lensed) background galaxies; by contrast, the best-fit de Vaucouleurs or Sérsic (1968) models in many cases leave systematic residuals at count levels comparable to those of the relatively faint strongly lensed features.

In this work, we use radial B-spline models not only to generate residual images, but also as the basis for aperture photometry and light-traces-mass lens models (see §5.2 below). Motivated by this goal, we implement the modeling in a somewhat different manner than in Paper I, incorporating an overall isophotal ellipticity and solving for PSF-deconvolved models. Specifically, we define a generalized elliptical radial coordinate,

$$R_{\text{ell}} = \sqrt{qx^2 + y^2/q}, \quad (1)$$

where the  $(x, y)$  coordinate system has the lens galaxy center at its origin and is aligned with the principal axes of the galaxy image. The lens-galaxy light profile is then modeled as a B-spline function of  $R_{\text{ell}}$  as described in Paper I, with the lens-galaxy isophotal axis ratio  $q$ , the position of the lens center  $(x_c, y_c)$ , and the major-axis position angle of the galaxy image (measured E from N) as non-linear model parameters in addition to the linear B-spline coefficient amplitudes. For a given trial choice of the non-linear parameters, basis images corresponding to the B-spline coefficients are generated and convolved with the appropriate PSF, and the linear combination of these basis images that best fits the data is computed.

We perform the B-spline model fits to the sky-subtracted imaging data over a  $14'' \times 14''$  region centered on the target lens candidate galaxies. The box size is chosen primarily to extend well beyond the scale of all lensed features and half-light radii. Before fitting, we manually generate masks for stars, neighboring galaxies, and possible lensed features so as to exclude those pixels from the fits. The initial B-spline modeling includes no higher-order multipole terms, and solves for the non-linear parameters by minimizing the  $\chi^2$  statistic using the IDL MPFIT implementation of the Levenberg-Marquardt algorithm (Moré & Wright 1993). The residual images produced by subtracting these initial models are then examined, and the masks are manually grown to exclude features not flagged in the original images. A second round of B-spline models is then computed by fixing the non-linear parameters and allowing for the following combinations of multipole terms in the fit: none, quadrupole, quadrupole+octopole, dipole, dipole+quadrupole. The inclusion of these terms allows the model to fit the effects of diskiness/boxiness, isophotal twist, variable ellipticity with radius, and an imperfect PSF model. We inspect the residual images generated by subtracting these model fits and select a particular multipole combination. Models are preferred in the order given in the preceding list, with later models being adopted only if they provide visibly significant improvement over earlier models. The inclusion of dipole terms is necessary for some systems in order to model slight asymmetry in the galaxy image. A small number of systems (mostly edge-on S0s) require multipole orders beyond the simple list; those systems are handled separately, with additional multipole orders added until the residual images are satisfactory for strong-lensing analysis. This special handling is only done for systems whose direct images show possible evidence of strong lensing (see Figures 5 and 6 in Appendix A).

#### 4.2. De Vaucouleurs analysis

To compute standardized model magnitudes, effective radii  $R_e$ , and projected axis ratios of the SLACS targets, we fit the images with two-dimensional ellipsoidal de Vaucouleurs luminosity profiles. These fits are performed over a  $51'' \times 51''$  square region centered on the target galaxies (approximately half the narrower dimension of the WF1 CCD aperture in which the targets were roughly centered). The manually created masks from the B-spline stage are applied in the central regions; stars and neighboring galaxies outside the manually masked area are masked from the de Vaucouleurs fit with a single-step “clipping” of pixels that deviate by more than 4

sigma higher than the model. The fits are performed using the MPFIT2DFUN procedure in IDL, and include convolution with the appropriate rectified and stacked Tiny Tim PSF. The initial optimization is done by sampling the model at one point per data pixel; a final optimization is done with  $5 \times 5$  sub-sampling per pixel. Model magnitudes are computed from the full (not truncated) analytic integral of the best-fit de Vaucouleurs model. Effective radii are quoted at the intermediate axis: i.e., the geometric mean of the major and minor axes of the elliptical isophotal contour enclosing one-half the model flux.

To test for bias in the de Vaucouleurs model-based magnitude measurements, we compare to aperture fluxes evaluated using the more general B-spline luminosity-profile models of §4.1. We consider an aperture defined by twice the de Vaucouleurs effective radius, which in the de Vaucouleurs case encloses 69% of the total model flux. We exclude ten galaxies whose effective radius exceeds the range modeled by the B-spline method above. The mean fractional difference (B-spline minus de Vaucouleurs) in aperture flux values across the sample is 1.0%, with an RMS difference of 2.3%. Thus we see that the de Vaucouleurs magnitudes are in good agreement with magnitudes determined through less parametric methods.

In order to obtain rest-frame photometric quantities, we apply several corrections to the observed  $I$ -band magnitudes. We apply corrections for Galactic dust extinction using the values of Schlegel, Finkbeiner, & Davis (1998). We also apply  $k$ -corrections to transform observed  $I$ -band magnitudes to rest-frame  $V$ -band magnitudes: these two passbands are very well matched for the higher redshift SLACS lenses, and reasonably close in wavelength for the lower redshift lenses. Since multi-band observations are not available for the full target sample, and since the SDSS colors will in general be affected by contributions from the background galaxies, we apply a single redshift-dependent  $k$ -correction based upon a single-burst synthetic stellar population (Bruzual & Charlot 2003), as described in Treu et al. (2001b). These same  $k$ -corrections were used in the analysis of Paper IV, and should be well suited to the old stellar populations found in the SLACS lenses (see Paper II). We expect these  $k$ -corrections to be accurate to better than 0.05 mag (MacArthur et al. 2007). Forthcoming multi-band  $HST$  photometry for the full SLACS lens sample will permit measurement of lens-galaxy colors separately from those of the background galaxies, thus enabling the most accurate  $k$ -corrections. The  $k$  corrections applied in B07 included a computational error that has been corrected in the current analysis (and that does not alter the conclusions of that work, as can be seen in Paper VII). We derive corrections to absolute luminosity using the adopted  $(\Omega_M, \Omega_\Lambda, h) = (0.3, 0.7, 0.7)$  FRW cosmology. Finally, we correct for luminosity evolution in the sample assuming a rate of  $d \log L_V / dz = 0.4$  (Kelson et al. 2000b; Treu et al. 2001a; Moran et al. 2005), derived from the evolution of the fundamental plane relationship (FP Dressler et al. 1987; Djorgovski & Davis 1987). Ideally we would like to constrain this evolution rate directly within the SLACS sample, but the sample probes systematically more massive and luminous galaxies at higher

redshift, and thus evolutionary trends are significantly covariant with mass/luminosity trends (see Figure 1 in §5.1 below). The evolution correction that we apply here is the same as was adopted in Paper IV, though here we correct luminosities to  $z = 0$  rather than  $z = 0.2$ . In either case, the RMS variation about the sample mean luminosity correction is on the order of a few hundredths dex, since the SLACS sample does not span an especially wide range in redshift. The measured photometric parameters for the full SLACS target sample are presented in Table 4 (in Appendix A), along with SDSS names/coordinates, redshifts, and velocity dispersions.

## 5. STRONG LENSING ANALYSIS

This section presents the details of our strong-lensing analysis. The first evidence in support of the strong-lensing hypothesis is the presence of two distinct galaxy redshifts within the same SDSS spectrum, covering a  $3''$  diameter spatial region, which forms the basis of our *HST*-ACS target selection. Further evidence is provided by the appearance of features characteristic of strong lensing in our high-resolution *HST* follow-up imaging, by successful quantitative strong-lensing models of those features, and in some cases by spatially resolve spectroscopy of the background-redshift emission-line flux.

### 5.1. Classification and sample overview

The classification of observed candidates into lenses and non-lenses is made by visual examination of the direct and B-spline model-subtracted residual images in all available *HST*-ACS bands, based on the appearance of arcs, rings, and multiple images centered on the position of the foreground galaxy. Initially, this classification is made independently by three different subsets of the authors (ASB, RG, and LVEK + TT). Out of the systems selected as definite lenses by any one individual initial judgment, the percentage of unanimously agreed-upon definite lenses ranges from 77% to 87%. Subsequently, all systems are inspected simultaneously by a single group of authors (ASB + LVEK + TT + LAM), and a consensus classification into definite lenses (“grade A”), possible lenses (“grade B”), and non-lenses or systems of unknown status (“grade X”) is decided, additionally taking into account integral-field spectroscopic evidence where available (see below). In the case of grade-A systems, the ACS direct and residual images show clear evidence of multiple imaging of a background galaxy consistent with general strong-lensing geometries. For grade B systems, the ACS data show evidence of probable multiple imaging, but have either a signal-to-noise ratio (SNR) too low for reliable lens modeling and definitive conclusion, or some degree of ambiguity in the identification of lensed features. We anticipate that the majority of the grade-B systems will be promoted to grade-A upon the completion of deeper imaging in multiple bands. Grade X is a catch-all classification that includes systems where the background galaxy is only singly imaged (i.e., positioned at large impact parameter relative to the foreground galaxy) and systems where the likely source of background-redshift line emission is either undetected or very weakly detected in the ACS imaging. In principle, grade-X systems with a background galaxy at large impact parameter are also a matter of insufficient SNR,

TABLE 1  
SUMMARY OF SLACS LENS DISCOVERY PROGRAMS (ACS ONLY)

Program Number	Grade-A Lenses	Grade-B Lenses	Grade-X Systems
10174	26	5	8
10587	16	10	28
10886	28	4	6
Total	70	19	42

since at arbitrary imaging depth some part of any background galaxy may be seen to be strongly lensed. However, practical confirmation and measurement seems out of reach for these systems. The consensus classifications of all ACS targets are given in Table 4 in Appendix A. Out of a total of 131 successfully observed targets, we confirm a total of 70 grade-A lenses, 19 grade-B lenses, and 42 non-lenses (grade X). The numerical breakdown of lenses confirmed in each of the three discovery programs (#10174, #10587, and #10886) is presented in Table 1.

Figure 1 shows the distribution of SLACS targets and confirmed lenses in redshift, velocity dispersion, and luminosity. One can see the significant covariance between magnitude and redshift—fundamentally a consequence of the SDSS spectroscopic target selection—that prevents us from using the SLACS lens sample to track the evolution of a single population across redshift. We must rather assume a rate of luminosity evolution as we have done here, or alternatively assume that the sample evolves onto the locally observed FP relation at redshift  $z = 0$ . This latter approach will be feasible once multi-band photometry of the SLACS lens sample is complete.

One of the powerful aspects of the selection of SLACS targets from within the SDSS spectroscopic database is the ability to estimate the angular lensing Einstein radius  $b$  (and hence the strong-lensing cross section) of candidates before follow-up observation. This is possible through the combination of foreground and background spectroscopic redshifts with measured SDSS velocity dispersions and a simple singular isothermal sphere model as per Equation 2. The conversion from lensing *cross section* to lensing *probability* requires a knowledge of the distribution of background galaxies in size and luminosity, as well as an accounting for the footprint of the SDSS fiber projected back into the un-lensed background plane (which depends upon the lens strength). Nevertheless, the probability that a source is a strong lens should be an increasing function of strong-lensing cross section and hence of predicted Einstein radius. Figure 2 shows this effect for the SLACS targets with well-measured SDSS velocity dispersions. We see a rise from a  $\approx 20\%$  confirmation at a predicted  $b$  of  $0''.5$  up to a  $\approx 100\%$  confirmation rate at a predicted  $b$  of  $2''$ .

In some cases, spatially resolved integral-field unit (IFU) spectroscopy of SLACS targets is available from a separate survey program using the Magellan and Gemini telescopes. The details of this IFU survey, along with narrow-band images extracted from the IFU data cubes showing the spatial morphology of the background line emission, are presented by Bolton & Burles (2007). A subset of these IFU data were also presented in Paper I, showing how the spatial coincidence between putative

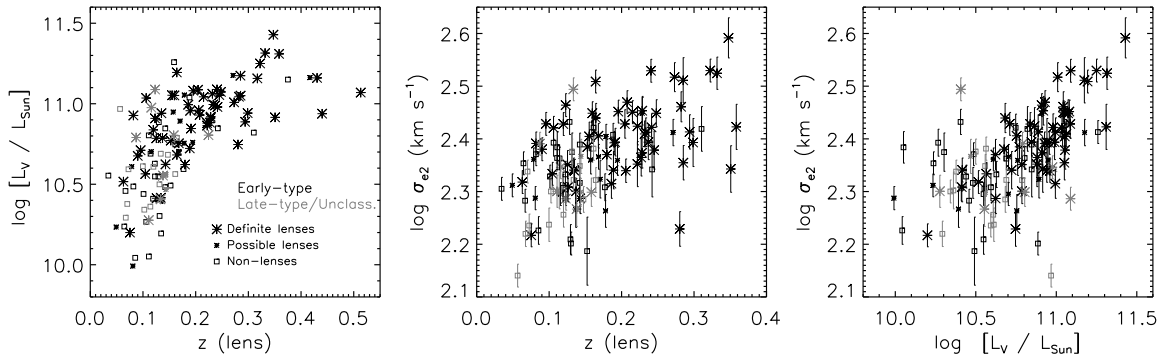


FIG. 1.— Joint distribution of ACS targets in redshift, luminosity, and velocity dispersion.

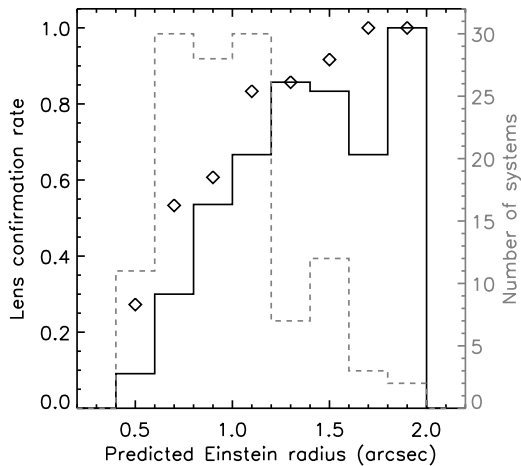


FIG. 2.— SLACS lens confirmation rate as a function of predicted Einstein radius  $\theta_E$ . Values for  $\theta_E$  are computed from foreground and background galaxy redshifts and velocity dispersions, all measured from SDSS spectroscopy, in combination with a singular isothermal sphere galaxy model. Only systems with a median SNR of 10 or more per  $69\text{-km s}^{-1}$  pixel over the rest-frame range  $4100\text{\AA}$  to  $6800\text{\AA}$  are considered here, so as to ensure well-measured velocity dispersions. Solid black line shows lens confirmation rate (left-hand ordinate) for grade “A” lenses, while black diamonds indicate the confirmation rate for grade “A” and “B” lenses combined. Dashed gray line shows total number of targeted systems in each bin (right-hand ordinate).

lensed features in the *HST* imaging and high-redshift emission-line flux in the IFU data can solidify the strong-lens hypothesis. The full list of SLACS targets with Magellan and Gemini IFU spectroscopy is presented in Table 2, along with brief comments on the implications of the IFU data for the interpretation of the *HST* imaging. A separate program to obtain VLT IFU spectroscopy (at lower spatial resolution but higher SNR) is described in Czoske et al. (2008).

### 5.2. Mass modeling

Here we describe our strong-lens mass modeling procedure and results. Construction of a successful strong gravitational lens model is necessary both to solidify the lensing hypothesis in a candidate lens system and to make the lens-mass measurements of scientific interest. Lens models must simultaneously describe the distribution of light in the un-lensed background “source plane” and the distribution of mass in the foreground

“lens plane” that generates the gravitational potential through which the source plane is viewed.

For all systems classified as grade-A lenses, we fit the putative lensed images with a singular isothermal ellipsoid (SIE) lens model (Kormann et al. 1994; Kassiola & Kovner 1993; Keeton & Kochanek 1998). The SIE model consists of similar concentric and aligned elliptical isodensity contours with axis ratio  $q_{\text{SIE}}$ . In the circular ( $q = 1$ ) limit, the projected surface density of the SIE falls off as  $\Sigma \propto R^{-1}$  in two dimensions. The model is parameterized by its angular Einstein radius  $b$ , which is related to the physical mass model through

$$b = 4\pi \frac{\sigma_{\text{SIE}}^2}{c^2} \frac{D_{LS}}{D_S}. \quad (2)$$

Here,  $\sigma_{\text{SIE}}$  is a velocity-dispersion parameter and  $D_{LS}$  and  $D_S$  are cosmological angular-diameter distances from lens to source and observer to source respectively. As in previous SLACS papers, we adopt the intermediate-axis normalization of Kormann et al. (1994), whereby the mass within a given isodensity contour remains constant at fixed  $b$  for changing axis ratio  $q_{\text{SIE}}$ . We model the lensed background galaxies as either single or multiple Gaussian or Sérsic ellipsoid components as necessary to obtain a good fit. The center of the mass model is constrained to be coincident with the center of the lens-galaxy light profile. Initial trial values for the lens-model Einstein radius and axis ratio are taken from the separation of the candidate lensed images and from the ellipticity of the light profile. The model lensed image is generated by ray-tracing through the analytic SIE mass model to view the parameterized source galaxy model, and subsequently convolved with the ACS PSF. All model parameters (lens and source) are adjusted manually to approximately match the data, and are then optimized using MPFIT. The final outcome is a set of lens-model and source-component parameters, along with a model for the lensed image configuration. This parametric source-plane technique (also employed by B07 and Marshall et al. 2007) can be contrasted with the pixellated source-plane techniques for modeling resolved optical sources described by Warren & Dye (2003), Treu & Koopmans (2004), Wayth & Webster (2006), and Paper III. We employ the parameterized strategy for its simplicity and ease of implementation, and for the robustness of the resulting aperture-mass measurements. Future work will apply the

TABLE 2  
SUMMARY OF MAGELLAN/GEMINI INTEGRAL-FIELD SPECTROSCOPIC EVIDENCE FOR/AGAINST LENSING IN SLACS SYSTEMS

System Name	Comments on IFU+ <i>HST</i> Data
SDSSJ0037–0942	Clear coincidence of IFU line emission and <i>HST</i> lensed features
SDSSJ0044+0113	Clear coincidence of IFU line emission and <i>HST</i> lensed features
SDSSJ0737+3216	Clear coincidence of IFU line emission and <i>HST</i> lensed features
SDSSJ0956+5100	Low-SNR IFU line emission coincident with <i>HST</i> lensed features
SDSSJ1029+6115	Lensed galaxy rotation curve in IFU data; <i>HST</i> imaging ambiguous.
SDSSJ1155+6237	IFU shows emission-line source not multiply imaged, despite multiple <i>HST</i> .
SDSSJ1259+6134	Low-SNR possible lensing features in IFU and <i>HST</i> ; very inconclusive
SDSSJ1402+6321	Clear coincidence of line emission and <i>HST</i> lensed features
SDSSJ1416+5136	Clear coincidence of IFU line emission and <i>HST</i> lensed features
SDSSJ1630+4520	Clear coincidence of IFU line emission and <i>HST</i> lensed features
SDSSJ1702+3320	Low-SNR possible lensing features in IFU and <i>HST</i> ; inconclusive
SDSSJ2238–0754	Clear coincidence of line emission and <i>HST</i> lensed features
SDSSJ2302–0840	Clear lensed ring in IFU data; <i>HST</i> imaging ambiguous.
SDSSJ2321–0939	Clear coincidence of line emission and <i>HST</i> lensed features

pixellated source-plane method to the full SLACS lens sample.

Figure 6 and Table 5 in Appendix A present the best-fit lens-model images and parameters that result from this modeling procedure. With the exception of the systems listed in Table 6 of Appendix A (which all involve complicating factors as described), the SIE analysis yields successful models of the lensed surface-brightness distribution. In certain cases we see data–model mismatch at the level of detailed features, as is to be expected given the parameterization of the source-plane surface-brightness distribution in terms of Gaussian and Sérsic ellipsoids. This outcome confirms the essential validity of our visual classifications: the trained eye is in fact quite good at “mental modeling” and hypothesis testing in strong lensing.

It is worth noting that the SIE lens modeling succeeds with the peak of the mass distribution constrained to be coincident with the peak of the luminosity profile. This is consistent with stellar mass being the dominant contributor to the gravitational field in the central kiloparsecs, and requires that the dark-matter component and any significant gas mass be well aligned with the stellar spheroid. Furthermore, this coincidence requires that the SLACS lenses must be located at or very near to the center of mass of any environmental overdensities (groups/clusters) in which they may be located. We can quantify the extent of the average mass-light centroid coincidence by continuing the lens-model optimization while freeing the mass centroid to move in position. For this analysis, we identify a subset of 32 grade-A lenses that are either complete or nearly complete “Einstein rings” with relatively high SNR lensed features, which we refer to as the “ring subset” and which are identified in Table 5 (in Appendix A). Since the lensed images in this subset extend through a large range in azimuth about the lens center, the mass centroids of the lens models are especially well constrained. We find an RMS shift of the mass centroid of 0′.044—approximately one native ACS pixel. Such shifts are probably small enough to be consistent with no shift at all, given the many accumulated sources of minor uncertainty. Converting the shifts to physical scales at the lens redshifts, the RMS mass centroid shift is 140 parsecs. As a fraction of the measured Einstein radii, the RMS shift is 3.5%. The quantitative

implications of this positional mass–light alignment will be explored in a future SLACS publication.

In most scientific applications of strong lensing, measured Einstein radii are of primary interest, providing direct determinations of the enclosed mass. In the case of Einstein ring images or symmetric quadruple-image lenses, this aperture-mass measurement is nearly independent of the radial density profile of the adopted lens model (Kochanek 1991). When the lensed image configuration is significantly asymmetric, the Einstein radius parameter measured from the data becomes somewhat dependent on the assumed mass model (e.g., Rusin et al. 2003). To assess the magnitude of this effect in the SLACS sample, we also fit all SIE-modeled systems with light-traces-mass (LTM) lens models derived from the B-spline galaxy models. We use the deconvolved B-spline ellipsoid model with no multipole dependence, since the higher-order models needed to produce the best residual images are in some cases unstable under deconvolution. We compute the lensing deflection of the LTM models directly from the deconvolved B-spline model images using fast Fourier techniques (e.g., Wayth & Webster 2006), and take the overall mass-to-light ratio for each system as a free parameter analogous to the Einstein radius parameter of the SIE model. We also include an external shear and its position angle as free parameters, in order to allow for angular degrees of freedom analogous to the free axis ratio and position-angle parameters of the SIE, which are necessary in order to obtain reasonable fits (e.g. Keeton et al. 1997). In a comparative sense, this can give a slight advantage to the LTM over the SIE models, since the former can model both an internal quadrupole moment (through the fixed ellipticity of the light profile) and an external quadrupole moment (through the shear). In the majority of cases, however, the best-fit SIE and LTM model images for the lensed features are visually indistinguishable from one another. We note however that the results of Paper III (based on combined lensing and dynamical models), Paper IV (based on combined strong- and weak-lensing analysis), Paper VI (for the double Einstein ring SDSSJ0946+1006), and Paper VII (based on homologous ensemble strong-lensing analysis) strongly favor the SIE radial mass-density profile over the LTM profile for the SLACS lens sample (also see Koopmans & Treu 2002,

2003; Treu & Koopmans 2002, 2003, 2004, Rusin et al. 2003; Rusin & Kochanek 2005). We convert the fitted LTM mass-to-light ratios into LTM Einstein radii by determining the radial position at which the lensing deflection of the best-fit LTM mass model exactly matches the radial offset from the lens center in the circular limit. The LTM mass model parameters are given in Table 5, and the model images can be seen along with the SIE model images in Figure 6 (all within Appendix A). These LTM lens models are used alongside the SIE models in Paper VII to assess the dependence of the derived physical scaling relations upon the assumed form of the lensing mass model.

## 6. MEASUREMENT COMPARISONS AND ERRORS

In this section we compare our mass and light parameter measurements to values obtained for the same systems through different procedures. This provides both a sanity check and a more realistic sense of the measurement errors associated with the individual parameters. Formal statistical errors can be obtained from the parameter covariance matrices (evaluated at the best-fit parameter values in the case of non-linear fits), but these estimates only account for the contribution of photon-noise and read-noise to the error budget, and they only apply to the idealized case where the true luminosity and mass distributions under study are exactly of the forms described by the parameterized models. Though the system-by-system uncertainties in all quantities of interest will in general depend upon the details of the lensed image configuration in that system and upon the depth of observation, subsequent work will benefit from the determination of the typical realistic uncertainty across the sample in each measured parameter. In particular, the empirical scaling-relation analyses of Paper VII employ the estimates of characteristic errors that we derive here. Table 3 presents a summary of the formal statistical errors and the adopted empirical errors derived from the analysis of this section.

### 6.1. Mass model parameters

First we compare our SIE Einstein radius measurements with those measured for subsets of SLACS lenses in Paper III (14 systems in common) and Paper IV (13 systems in common), as well as with the measurements made for B07 (34 systems in common). The lens modeling of Paper III and Paper IV was carried out with a regularized pixellated source plane as opposed to the multi-Sérsic models of this work. The models of B07, meanwhile, were parameterized in the same manner as in the current work, but were fitted directly to the native pixel data of single Snapshot exposures, rather than to the rectified (and in some cases combined) frames used in this work. We also note that the values published in Table 1 of Paper IV reflect an error in the conversion from major-axis to intermediate-axis conventions, and should be divided by the square-root of the mass axis ratio to provide for a proper comparison to the values of this paper. The corrections are small, and we have verified that the results and conclusions of Paper IV are not significantly altered by the change. Figure 3 shows the fractional difference between SIE Einstein radii measured by different methods for the same systems, as a function of SIE Einstein radius  $b$ . The RMS fractional

differences are 2% for Paper III and B07 relative to the current work, with no significant systematic bias. Relative to this work, the values of Paper IV exhibit a larger 6% fractional scatter, though this reduces to 3% with no significant systematic offset if the two outlying systems J0728 and J0841 are excluded. With regard to these two systems: J0728 shows complex lensing morphology that may admit qualitatively different lens-model interpretations, while J0841 is a highly asymmetric double-image lens, for which the measured Einstein radius can be more significantly degenerate with a combination of mass axis ratio and position angle. In subsequent analyses, we will adopt a 2% RMS fractional error as our best estimate of the uncertainty on measured Einstein radii. For comparison, the median formal statistical error for the 63 Einstein-radius measurements given in this paper is 0.2%.

We also wish to determine the actual error in the lensing measurements of the projected mass axis ratio and major-axis position angle through comparison of current measurements to the SIE models of B07. For the minor-to-major projected mass axis ratio  $q_{\text{SIE}}$  (which ranges between 0 and 1), we find an RMS difference of 0.05 with no significant systematic bias. We will adopt 0.05 as our typical parameter uncertainty, which contrasts with the much smaller median formal statistical error in  $q_{\text{SIE}}$  of 0.005. Comparing position-angle measurements, we find a mean difference (B07 minus this work) of  $0.8^\circ \pm 1.0^\circ$ —consistent with no systematic misalignment—with an RMS difference of  $5.7^\circ$ , after rejecting three outlier systems with large position-angle differences between the two works. Even in these outlier cases (J0935–0003, J1204+0358, and J1403+0006), the Einstein-radius measurements between the two works agree to within 5%, a fact which highlights the relative robustness of the Einstein radius among lens parameter measurements. For the ring subset defined in §5.2—for which the angular mass properties are especially well constrained—the RMS position-angle difference (B07 minus this work) is a much smaller  $2.0^\circ$ . Thus we see that a  $2^\circ$ – $6^\circ$  RMS statistical uncertainty applies for the measured mass position angles, though we recognize that catastrophic outliers may creep in. For comparison, the median formal statistical error in the measured mass position angles is less than  $1^\circ$ .

### 6.2. Surface-brightness model parameters

Next we compare multiple F814W de Vaucouleurs surface photometry measurements for the same target galaxies. Perhaps the best check of purely “statistical” (though not photon-counting) photometric errors is obtained through comparison of magnitudes measured for the 16 systems with both Snapshot (discovery) and full-orbit (follow-up) observations through the same filter. In this case, the mean offset (snapshot minus full-orbit) is  $-0.01$  magnitude, with an RMS offset of 0.03 magnitude. For comparison, the formal statistical error estimates for these measurements are at the level of one to two millimagnitudes. We will adopt this value of 0.03 magnitudes as our photometric error estimate for all systems. Though the full-orbit measurements should arguably be given smaller errors, we do not wish to over-weight the 43 lens systems with full-orbit F814W photometry relative to the 20 with only Snapshot measurements (and in



TABLE 3  
FORMAL AND EMPIRICAL MEASUREMENT-ERROR ESTIMATES

Measured Quantity	Formal Statistical Error	Adopted Empirical Error
Einstein radius $b$	0.2%	2%
Mass axis ratio $q_{\text{SIE}}$	0.005	0.05
Mass position angle	$< 1^\circ$	$6^\circ$ ( $2^\circ$ for ring subset)
De Vauc. magnitude	0.001–0.002 mag	0.03 mag
Effective radius $R_e$	$< 0.2\%$	3.5%
Velocity dispersion	7%	7%

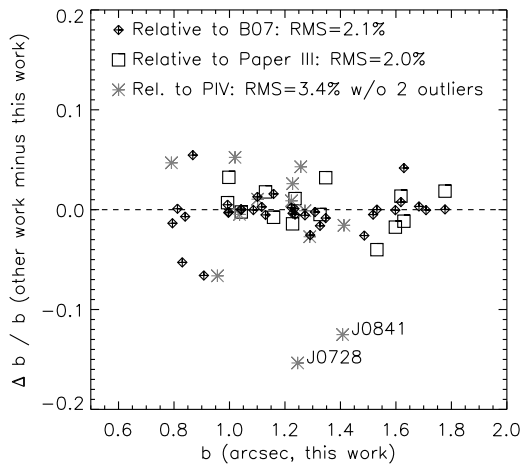


FIG. 3.— Fractional difference between SIE Einstein radii  $b$  from the analyses of other SLACS papers and this work.

any event, the dominant magnitude errors are not set by the observation depth).

The measurements made and published previously in the SLACS series have used slightly different model-fitting procedures, and the resulting dispersion in values provides a further check on our levels of statistical and systematic confidence. The closest comparison is to the Snapshot photometry of 15 systems in Paper II, for which the reduction, masking, and fitting procedures were most similar (though not identical) to the current methods. We find a mean offset (Paper II minus this work) of  $-0.026$  magnitudes and an RMS difference of  $0.047$  magnitudes. Comparing next to 21 photometric values published in Paper IV, we find a mean offset (Paper IV minus this work) of  $-0.013$  and an RMS difference of  $0.2$  magnitudes.<sup>11</sup> The Paper IV values were taken from models fitted to a significantly smaller region ( $24''$  to a side, versus the  $54''$  to a side used in this work), and the Paper IV masking procedure was fully automated whereas this work applies manual masks in the inner  $14'' \times 14''$ . Paper IV measurements also included a free diskiness/boxiness parameter whereas the models of the current work are pure ellipsoids. Thus we interpret the scatter between these two sets of magnitudes as evidence of the well-known effect that de Vaucouleurs magnitude of a galaxy depends both on the galaxy itself and upon the fitting procedure used, due to departures of the real galaxy from the simple de Vaucouleurs ellipsoid form. While this could perhaps be mitigated by the use of

<sup>11</sup> The apparent F814W magnitude for SDSSJ1023+4230 as published in Paper IV should read 16.93. The Paper IV *absolute* magnitude of this galaxy is correct as printed.

the Sérsic model, the extrapolated flux in the low-surface brightness wings of the Sérsic model is highly dependent upon the Sérsic index  $n$ , and becomes quite a large fraction of the total model flux when  $n$  becomes large. Use of Sérsic magnitudes would also greatly complicate comparison with other studies based upon de Vaucouleurs photometry. Thus we work with de Vaucouleurs magnitudes here and in the scaling-relation analyses of Paper VII.

We also compare de Vaucouleurs effective (half-light) radius measurements—taken from the same model fits as the magnitudes—from multiple measurement procedures. Comparing Snapshot to full-orbit measurements as above, we find a mean fractional offset (Snapshot minus full orbit) of  $1\%$  and an RMS difference of  $3.5\%$ ; we will adopt this value as our empirical error estimate going forward. The median formal fractional statistical error in the effective radius measurements, by comparison, is less than two tenths of one percent. Comparing the Snapshot measurements of this work to those of Paper II (converting the latter from a major-axis to an intermediate-axis convention), we find a mean offset (Paper II minus this work) of  $0.1\%$  and an RMS difference of  $5\%$ . Comparing to Paper IV values, we find a mean difference (Paper IV minus this work) of  $0.5\%$  and an RMS difference of  $25\%$ . The significant scatter between current and Paper IV values we again attribute to the significant differences in analysis procedures. Finally, we compare the values measured in the current work to  $i$ -band de Vaucouleurs effective radii from the SDSS photometric database (converting SDSS values from major axis to intermediate axis). Excluding the 6 systems with multiple foreground-galaxy multiplicities, and rejecting a further 6 outlier systems (leaving a sample of 119 total), we find a mean offset (SDSS minus this work) of  $-0.7\%$  and an RMS difference of  $12\%$ . Again, we note that the de Vaucouleurs effective radius depends largely upon the analysis details. Similar scatter in the precise determination of effective radii has been found by (Kelson et al. 2000a) and Treu et al. (2001b).

Since errors on the de Vaucouleurs magnitudes and effective radii are significantly correlated, we also derive an empirical error in the effective surface brightness, proportional to the model luminosity divided by the square of the model effective radius. From the comparison of Snapshot to full-orbit measurements of this quantity, we find an RMS fractional difference of  $4.5\%$ , which we will adopt as our empirical uncertainty in the measured effective surface brightnesses.

### 6.3. Velocity-dispersion measurements

The stellar velocity dispersion measurements that we present in this paper and use extensively in Paper VII are measured from SDSS spectroscopic data by the Prince-

ton/MIT analysis pipeline.<sup>12</sup> The SDSS spectrograph fibers sample a seeing-convolved circular spatial aperture of  $3''$  in diameter centered on the target galaxies. The median seeing is  $\approx 1''.4$ ; the physical scale of the fiber diameter is about 10 kpc at a redshift of  $z = 0.2$ . Velocity dispersions are measured by fitting a linear combination of stellar templates to the observed galaxy data in pixel space, weighted using the estimated observational errors and masking pixels at common emission-line wavelengths. All templates are shifted together by a free velocity-shift parameter (initialized using the primary galaxy-redshift value), and broadened by a single Gaussian kernel described by a free velocity-dispersion parameter (in addition to broadening by the fixed spectrograph resolution). A grid of trial velocity-dispersion and velocity-shift parameters is explored, and the corresponding  $\chi^2$  values are mapped out by optimizing the stellar template coefficients linearly at each grid point. The best-fit velocity dispersion is derived at the  $\chi^2$  minimum of a quadratic fit to those points near the minimum in the grid values. The stellar templates themselves are derived from a principal-components analysis of the original ELODIE library of high-resolution stellar spectra (Prugniel & Soubiran 2001), keeping the 24 most significant eigenvectors from 886 of the 908 stars The ELODIE spectra cover the rest-frame wavelength range 4100–6800 Å. For analyses that make use of these velocity dispersions, we only consider the subset of foreground galaxies with median spectral SNR of 10 or greater per  $69 \text{ km s}^{-1}$  pixel over this wavelength range. This prevents the inclusion of velocity-dispersion data points with excessively (or catastrophically) large errors.

Unlike most other measurements reported in this work, the SDSS velocity dispersions are generally in an SNR regime where the dominant contribution to the uncertainty is due to the statistics of photon counting. We test for any further random uncertainty by comparing the velocity dispersions measured from the same data by two different revisions of the Princeton/MIT pipeline—one run following SDSS-DR4 and one following SDSS-DR6. For all simple early-type systems observed by SLACS with sufficient SDSS spectroscopic SNR to permit a measurement, the velocity-dispersion values from the two different runs are consistent, with a reduced  $\chi^2$  of 0.77 across the sample. We thus adopt the formal statistical error estimates directly, though we limit the fractional error estimate for any one system to a minimum of 5% in view of the systematic errors associated with possible mismatch in the stellar templates used in the measurement. Where necessary, we adopt 7% as a single overall value for the uncertainty in all the velocity dispersion measurements, though this value will necessarily be an underestimate of some errors and an overestimate of others.

## 7. CONTROL-SAMPLE TESTS

As discussed in Papers I and II, our ability to generalize deductions from the SLACS lens sample to the larger population of early-type galaxies requires an understanding of our selection procedure and of any possible biases that procedure may introduce. In a nutshell, the SLACS target selection is for the following:

1. A quiescent spectrum of the target SDSS galaxy,
2. The presence of higher redshift emission lines in the SDSS spectrum, and
3. Appreciable lensing cross section as estimated from redshifts and stellar velocity dispersions.

For the resulting *lens* sample, an additional condition is

4. The detection of strongly lensed features in *HST* imaging.

Our approach here will be similar to that employed in Papers I and II: we replicate conditions 1 and 3 by constructing comparison samples for each target from the SDSS database by identifying galaxies with (roughly) the same redshift, spectral quiescence, and velocity dispersion. The massive data volume of the SDSS spectroscopic database allows us to construct our comparison samples by directly matching observed quantities, thus limiting sensitivity to additional corrections. Furthermore—and unlike the analyses of Papers I and II—we also require the comparison-sample galaxies to have nearly equal effective radii to the corresponding SLACS targets. The combination of velocity-dispersion and effective-radius constraints ensures that the comparison samples should be located at the same point on the fundamental plane as the SLACS galaxies. If conditions 2 and 4 work to make the SLACS target sample significantly biased or un-representative, this should manifest as a biased distribution in magnitudes for the SLACS galaxies relative to their control samples.

Our recipe for constructing the comparison samples is summarized as follows. We work with the SDSS DR6 photometric and spectroscopic catalog (Adelman-McCarthy et al. 2007) so as to have the largest possible parent sample, with all data reduced by a single version of the SDSS photometric and spectroscopic pipelines. We select the overall parent sample by requiring a Princeton/MIT SDSS spectroscopic pipeline classification of *GALAXY* and a rest-frame  $H\alpha$  equivalent-width measurement of either less than 4 Å in value or less than 2 sigma in significance—conditions likewise required for SLACS target selection, with the exception of several late-type lenses and lens candidates. We also require that the best-fit spectroscopic pipeline template describe the spectrum with a reduced  $\chi^2$  of no more than 3, since a poor spectral model fit prevents the significant detection of higher-redshift emission lines in the model-subtracted residual spectrum. We impose a minimum median spectral SNR of 10 per pixel over the rest-frame range 4100–6800 Å. This SNR value is computed from the observed-frame *SN\_MEDIAN* reported by the Princeton/MIT pipeline through an empirical redshift-dependent conversion determined from the SDSS spectroscopy of the SLACS targets: the approximate rest-frame median SNR per pixel is given by  $\text{SN\_MEDIAN} + 20.4 \times z_{\text{lens}} - 1.24$ . Finally, we require that the SDSS *r*-band de Vaucouleurs effective radius be well measured, and that the magnitudes in all five SDSS filters also be well measured. For each SLACS target, we identify the subset of this parent sample within  $dz = \pm 0.01$  of the SLACS target redshift. We then identify a further subset with effective radii within  $\pm 7.5\%$  of the SLACS target

<sup>12</sup> <http://spectro.princeton.edu/>

value and with velocity dispersions in an interval containing the SLACS target value. The width of the velocity bin is set to 15% of the measured SLACS target velocity-dispersion value, and the bin center is chosen so as to give an equal number of comparison galaxies at higher and lower dispersion than the target. As noted in Paper II, a balancing of this sort is necessary due to the steepness of the velocity-dispersion function. For the confirmed SLACS lenses, the resulting comparison samples have from 26 to 2996 galaxies, with a median sample size of 666. These figures exclude the high velocity-dispersion lens SDSSJ0935–0003, which has only two comparison-sample galaxies (which are both brighter than the lens, by 0.1 and 0.5 magnitudes respectively).

With the comparison samples in hand for each SLACS target, we examine the distribution of SLACS magnitudes within these samples. We use SDSS values for the control samples as well as for the SLACS targets, so as to avoid complications of photometric zero-point matching. We reduce the SDSS fluxes of the modeled lenses by a percentage corresponding to the contribution of the lensed images to the total  $I$ -band flux within a seeing-convolved circle of radius  $3''$ , as measured from the *HST*-ACS data. For reference, we find an offset between ACS F814W de Vaucouleurs magnitude and SDSS  $i$ -band magnitude for the SLACS lenses given by  $i_{\text{SDSS}} - I_{814} = 0.17$ , with an RMS scatter of 0.19 magnitude. We compute absolute  $V$ -band magnitudes from the SDSS fluxes using distance moduli for our assumed cosmology and  $k$  corrections computed using the SDSS2BESSELL procedure of the `kcorrect` software (Blanton et al. 2003). We also apply our adopted luminosity-evolution correction, though it makes a difference of only  $\pm 0.01$  magnitude over the redshift width of the comparison-sample bins. For each SLACS target with a well-measured velocity dispersion, we then determine its rank within the cumulative distributions of absolute magnitude for its comparison sample. The rank values range from  $0.5/N_{\text{samp}}$  to  $1 - (0.5/N_{\text{samp}})$ , where  $N_{\text{samp}}$  is the number of galaxies in the comparison sample including the SLACS target. If the targets are drawn in a representative fashion from their parent samples, these ranks should be distributed uniformly between 0 and 1—a proposition we can test with the Kolmogorov-Smirnov (K-S) formalism. Figure 4 shows this K-S test of the absolute-magnitude rank distribution for the 52 early-type SLACS A-grade lenses with well-measured SDSS velocity dispersions (“lenses”, excluding SDSSJ0935–0003), as well as for the 41 other SLACS early-type target systems with single multiplicity and similarly well-measured velocity dispersions (“others”). The “lenses” are consistent with their parent samples at the 39.2% level, while the “others” are consistent with their parent samples at the 28.2% level. A two-sample K-S tests show that the two SLACS target populations (“lenses” and “others”) are consistent with one another in their distributions at the 39.0% level. We can also test for any systematic bias as a function of intrinsic lens-galaxy properties by testing for correlations between the absolute-magnitude rank of lenses within their control samples and their position within the  $R_e$ - $\sigma_{e2}$  plane. If any such correlations were present, then the SLACS lenses would define a biased FP relative to their control samples. In fact there are no such signif-

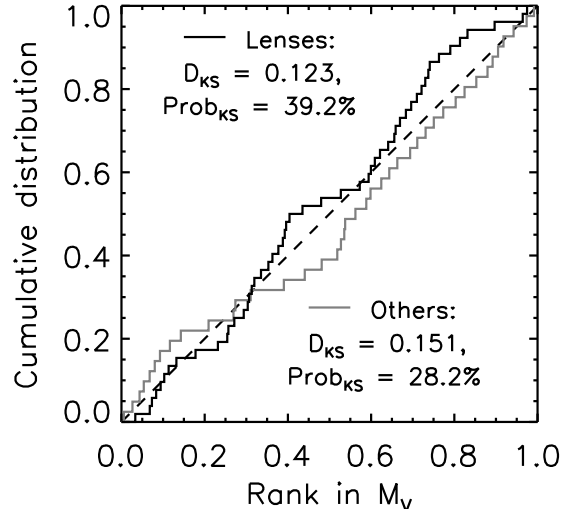


FIG. 4.— Kolmogorov-Smirnov (K-S) tests of the rank of 52 A-grade SLACS lenses and 41 other SLACS targets within the distributions of absolute magnitude  $M_V$  of their individual SDSS comparison samples. Only systems with single multiplicity, early-type morphology, and well-measured SDSS velocity dispersions are included. The null-hypothesis distribution—corresponding to a representative drawing of the SLACS systems from spectroscopically comparable galaxies in the SDSS—is given by the linear cumulative distribution shown with a dashed line. The K-S  $D$  statistic values are given, along with the probability of random occurrence of an equal or greater  $D$  value under the null hypothesis.

icant correlations: the linear correlation coefficient between magnitude-rank and effective radius (in physical units) is  $r = -0.080$ , and the correlation with velocity-dispersion is  $r = -0.088$ . The correlation of magnitude rank with the product  $\sigma_{e2}^2 R_e$  (proportional to the “dynamical mass” of the lens) is  $r = -0.065$ . From these tests we conclude that the SLACS lenses and other targets are statistically consistent with having been drawn at random from the parent SDSS galaxy population with similar spectroscopic properties.

## 8. SUMMARY AND CONCLUSIONS

We have presented an up-to-date catalog of the largest single confirmed strong gravitational lens sample to date, from the ACS data set of the SLACS Survey. The catalog includes 63 “grade-A” strong galaxy-galaxy lens systems complete with lens and source redshifts, F814W lens-galaxy photometry, gravitational lens models, and (in most cases) stellar velocity dispersions. Such a large and high-quality lens sample serves as a further proof-of-concept for the spectroscopic discovery channel, and provides a unique resource for the quantitative study of massive early-type galaxies. Many of the most immediate implications of our measurements for the structure and physical scaling relations of early-type galaxies are explored further in Paper VII.

We have described the details of the image-analysis and parameterized lens-modeling techniques that we use to make mass and luminosity measurements from the *HST*-ACS imaging data. Our analysis demonstrates that simple singular isothermal ellipsoid and light-traces-mass (plus external shear) lens models, combined with multiple Gaussian or Sérsic ellipsoid models of the lensed background galaxies, can reproduce the lensed image config-

urations in great detail. (More detailed modeling with pixellated source-plane surface-brightness distributions is currently being conducted to further reduce the level of systematic residuals and to extract all strong-lensing information.) The current models imply a precise positional alignment of the peaks of the mass and light distributions in the foreground lensing galaxies. We have also presented a realistic empirical analysis of the characteristic errors associated with the various measurements reported in this work, which are in general much larger than purely random-statistical considerations would indicate. Finally, we have demonstrated that the SLACS lens sample is statistically consistent with having been drawn at random from a parent population of similar galaxies from the SDSS, a conclusion that supports the generalization of SLACS results to the massive early-type galaxy population in general.

The strong lensing measurements presented in this work afford a unique opportunity to test the results of numerical simulations of galaxy formation, merging, and evolution. This is due to the fact that strong lensing measures total mass directly, in a nearly model-independent sense, and without need for modeling of stellar populations and luminosity evolution. One can envision a particularly simple test as follows. For a particular formation and merger-progenitor scenario, one can select simulated galaxies corresponding to each of the observed lens galaxies by identifying those with identical (or nearly identical) effective radii of the stellar tracer component (regardless of luminosity) and identical projected aperture masses within the physical Einstein radius of the lens. The line-of-sight velocity dispersions would then be computed for the simulated counterparts, and compared to the observed velocity dispersions of the lens galaxies. Through the level of agreement between these predicted and observed velocity dispersions across the full range of relevant scales, various formation scenarios could in principle be distinguished from one another. This amounts to a test of whether or not the simulated galaxies define the same mass plane—as defined in B07 and discussed further in Paper VII, in analogy to the fundamental plane—but through direct comparison with the data, rather than through the comparison of scaling-relation coefficients.

The main limitations to further quantitative study of the SLACS lens sample are due to (1) the observational error in the velocity dispersions derived from SDSS spectroscopy, and (2) the lack of high-resolution multi-color imaging of the full sample. To address the first limitation, follow-up spectroscopy of SLACS lenses is being pursued at the Keck and VLT observatories (Czoske et al. 2008). This spectroscopy additionally affords spatial resolution, allowing a direct measurement of the stellar kinematics within fixed physical apertures. The second limitation is being addressed through continued *HST* imaging of confirmed lenses in multiple bands,

which will allow quantitative study of the stellar populations within the SLACS lens galaxies and their lensed background source galaxies (Marshall et al. 2007).

ASB, TT, LVEK, RG, and LAM acknowledge the support and hospitality of the Kavli Institute for Theoretical Physics at UCSB, where a significant part of this work was completed. ASB thanks G. Dobler for valuable discussion related to this work. TT acknowledges support from the NSF through CAREER award NSF-0642621 and from the Sloan Foundation through a Sloan Research Fellowship. He is also supported by a Packard fellowship. LVEK is supported in part through an NWO-VIDI program subsidy (project number 639.042.505). He also acknowledges the continuing support by the European Community’s Sixth Framework Marie Curie Research Training Network Programme, Contract No. MRTN-CT-2004-505183 (“ANGLES”). The work of LAM was carried out at Jet Propulsion Laboratory, California Institute of Technology under a contract with NASA.

Support for *HST* programs #10174, #10494, #10587, #10798, and #10886 was provided by NASA through a grant from the Space Telescope Science Institute, which is operated by the Association of Universities for Research in Astronomy, Inc., under NASA contract NAS 5-26555. Please see *HST* data acknowledgment on title page.

This work has made extensive use of the Sloan Digital Sky Survey database. Funding for the SDSS and SDSS-II has been provided by the Alfred P. Sloan Foundation, the Participating Institutions, the National Science Foundation, the U.S. Department of Energy, the National Aeronautics and Space Administration, the Japanese Monbukagakusho, the Max Planck Society, and the Higher Education Funding Council for England. The SDSS Web Site is <http://www.sdss.org/>.

The SDSS is managed by the Astrophysical Research Consortium for the Participating Institutions. The Participating Institutions are the American Museum of Natural History, Astrophysical Institute Potsdam, University of Basel, University of Cambridge, Case Western Reserve University, University of Chicago, Drexel University, Fermilab, the Institute for Advanced Study, the Japan Participation Group, Johns Hopkins University, the Joint Institute for Nuclear Astrophysics, the Kavli Institute for Particle Astrophysics and Cosmology, the Korean Scientist Group, the Chinese Academy of Sciences (LAMOST), Los Alamos National Laboratory, the Max-Planck-Institute for Astronomy (MPIA), the Max-Planck-Institute for Astrophysics (MPA), New Mexico State University, Ohio State University, University of Pittsburgh, University of Portsmouth, Princeton University, the United States Naval Observatory, and the University of Washington.

## REFERENCES

- Adelman-McCarthy, J. K., et al. 2007, *ApJS*, in press (ArXiv 0707.3413)  
 Belokurov, V., et al. 2007, *ApJ*, 671, L9  
 Blackburne, J. A., Wisotzki, L., & Schechter, P. L. 2008, *AJ*, 135, 374  
 Blanton, M. R., et al. 2003, *AJ*, 125, 2348  
 Bolton, A. S., & Burles, S. 2007, *New J. Phys.*, 9, 443  
 Bolton, A. S., Burles, S., Koopmans, L. V. E., Treu, T., & Moustakas, L. A. 2005, *ApJ*, 624, L21  
 Bolton, A. S., Burles, S., Koopmans, L. V. E., Treu, T., & Moustakas, L. A. 2006, *ApJ*, 638, 703 (Paper I)  
 Bolton, A. S., Burles, S., Schlegel, D. J., Eisenstein, D. J., & Brinkmann, J. 2004, *AJ*, 127, 1860  
 Bolton, A. S., Burles, S., Treu, T., Koopmans, L. V. E., & Moustakas, L. A. 2007, *ApJ*, 665, L105 (B07)

- Bolton, A. S., et al. 2008, *ApJ*, in press (Paper VII)
- Browne, I. W. A., et al. 2003, *MNRAS*, 341, 13
- Bruzual, G., & Charlot, S. 2003, *MNRAS*, 344, 1000
- Cabanac, R. A., et al. 2007, *A&A*, 461, 813
- Czoske, O., Barnabè, M., Koopmans, L. V. E., Treu, T., & Bolton, A. S. 2008, *MNRAS*, 384, 987
- de Vaucouleurs, G. 1948, *Annales d’Astrophysique*, 11, 247
- Djorgovski, S., & Davis, M. 1987, *ApJ*, 313, 59
- Dressler, A., Lynden-Bell, D., Burstein, D., Davies, R. L., Faber, S. M., Terlevich, R., & Wegner, G. 1987, *ApJ*, 313, 42
- Eisenstein, D. J., et al. 2001, *AJ*, 122, 2267
- Fassnacht, C. D., Moustakas, L. A., Casertano, S., Ferguson, H. C., Lucas, R. A., & Park, Y. 2004, *ApJ*, 600, L155
- Faure, C., et al. 2008, *ApJ*, in press (arXiv:0802.2174)
- Fruchter, A. S., & Hook, R. N. 2002, *PASP*, 114, 144
- Gavazzi, R., et al. 2007, *ApJ*, 667, 176 (Paper IV)
- . 2008, *ApJ*, 677, 1046, (Paper VI)
- Gregg, M. D., et al. 2000, *AJ*, 119, 2535
- Griffith, M. R., & Wright, A. E. 1993, *AJ*, 105, 1666
- Hewett, P. C., Warren, S. J., Willis, J. P., Bland-Hawthorn, J., & Lewis, G. F. 2000, in *Astronomical Society of the Pacific Conference Series*, Vol. 195, *Imaging the Universe in Three Dimensions*, ed. W. van Breugel & J. Bland-Hawthorn, 94–104
- Inada, N., et al. 2007, *ArXiv e-prints*, 708
- Kassiola, A., & Kovner, I. 1993, *ApJ*, 417, 450
- Keeton, C. R., & Kochanek, C. S. 1998, *ApJ*, 495, 157
- Keeton, C. R., Kochanek, C. S., & Seljak, U. 1997, *ApJ*, 482, 604
- Kelson, D. D., Illingworth, G. D., van Dokkum, P. G., & Franx, M. 2000a, *ApJ*, 531, 137
- . 2000b, *ApJ*, 531, 184
- Kochanek, C. S. 1991, *ApJ*, 373, 354
- Koopmans, L. V. E., & Treu, T. 2002, *ApJ*, 568, L5
- . 2003, *ApJ*, 583, 606
- Koopmans, L. V. E., Treu, T., Bolton, A. S., Burles, S., & Moustakas, L. A. 2006, *ApJ*, 649, 599 (Paper III)
- Kormann, R., Schneider, P., & Bartelmann, M. 1994, *A&A*, 284, 285
- Krist, J. 1993, in *Astronomical Society of the Pacific Conference Series*, Vol. 52, *Astronomical Data Analysis Software and Systems II*, ed. R. J. Hanisch, R. J. V. Brissenden, & J. Barnes, 536–541
- Kubo, J. M., & Dell’Antonio, I. P. 2008, *MNRAS*, in press
- MacArthur, L. A., Ellis, R. S., Treu, T., U. V., Bundy, K., & Moran, S. M. 2007, *ApJ*, submitted (arXiv:0711.0238)
- Maoz, D., et al. 1993, *ApJ*, 409, 28
- Marshall, P. J., et al. 2007, *ApJ*, 671, 1196
- Miralda-Escude, J., & Lehar, J. 1992, *MNRAS*, 259, 31P
- Moran, S. M., Ellis, R. S., Treu, T., Smail, I., Dressler, A., Coil, A. L., & Smith, G. P. 2005, *ApJ*, 634, 977
- Moré, J. J., & Wright, S. J. 1993, *SIAM Frontiers in Applied Mathematics 14: Optimization Software Guide* (Society for Industrial and Applied Mathematics)
- Morgan, N. D., Gregg, M. D., Wisotzki, L., Becker, R., Maza, J., Schechter, P. L., & White, R. L. 2003, *AJ*, 126, 696
- Moustakas, L. A., et al. 2007, *ApJ*, 660, L31
- Myers, S. T., et al. 2003, *MNRAS*, 341, 1
- Oguri, M., et al. 2006, *AJ*, 132, 999
- . 2007, *ArXiv e-prints*, 708
- Prugniel, P., & Soubiran, C. 2001, *A&A*, 369, 1048
- Ratnatunga, K. U., Griffiths, R. E., & Ostrander, E. J. 1999, *AJ*, 117, 2010
- Rusin, D., & Kochanek, C. S. 2005, *ApJ*, 623, 666
- Rusin, D., Kochanek, C. S., & Keeton, C. R. 2003, *ApJ*, 595, 29
- Schlegel, D. J., Finkbeiner, D. P., & Davis, M. 1998, *ApJ*, 500, 525
- Sérsic, J. L. 1968, *Atlas de galaxias australes* (Cordoba, Argentina: Observatorio Astronomico, 1968)
- Strauss, M. A., et al. 2002, *AJ*, 124, 1810
- Treu, T., Koopmans, L. V., Bolton, A. S., Burles, S., & Moustakas, L. A. 2006, *ApJ*, 640, 662 (Paper II)
- Treu, T., & Koopmans, L. V. E. 2002, *ApJ*, 575, 87
- . 2003, *MNRAS*, 343, L29
- . 2004, *ApJ*, 611, 739
- Treu, T., Stiavelli, M., Bertin, G., Casertano, S., & Møller, P. 2001a, *MNRAS*, 326, 237
- Treu, T., Stiavelli, M., Møller, P., Casertano, S., & Bertin, G. 2001b, *MNRAS*, 326, 221
- van Dokkum, P. G. 2001, *PASP*, 113, 1420
- Warren, S. J., & Dye, S. 2003, *ApJ*, 590, 673
- Warren, S. J., Hewett, P. C., Lewis, G. F., Moller, P., Iovino, A., & Shaver, P. A. 1996, *MNRAS*, 278, 139
- Wayth, R. B., & Webster, R. L. 2006, *MNRAS*, 372, 1187
- Willis, J. P., Hewett, P. C., & Warren, S. J. 2005, *MNRAS*, 363, 1369
- Willis, J. P., Hewett, P. C., Warren, S. J., Dye, S., & Maddox, N. 2006, *MNRAS*, 369, 1521
- Winn, J. N., Lovell, J. E. J., Chen, H.-W., Fletcher, A. B., Hewitt, J. N., Patnaik, A. R., & Schechter, P. L. 2002a, *ApJ*, 564, 143
- Winn, J. N., et al. 2000, *AJ*, 120, 2868
- . 2001, *AJ*, 121, 1223
- . 2002b, *AJ*, 123, 10
- Wisotzki, L., Christlieb, N., Liu, M. C., Maza, J., Morgan, N. D., & Schechter, P. L. 1999, *A&A*, 348, L41
- Wisotzki, L., Koehler, T., Kayser, R., & Reimers, D. 1993, *A&A*, 278, L15
- Wisotzki, L., Koehler, T., Lopez, S., & Reimers, D. 1996, *A&A*, 315, L405+
- Wisotzki, L., Schechter, P. L., Bradt, H. V., Heinmüller, J., & Reimers, D. 2002, *A&A*, 395, 17
- Wisotzki, L., Schechter, P. L., Chen, H.-W., Richstone, D., Jahnke, K., Sánchez, S. F., & Reimers, D. 2004, *A&A*, 419, L31
- York, D. G., et al. 2000, *AJ*, 120, 1579

## APPENDIX

## DATA TABLES AND IMAGE FIGURES

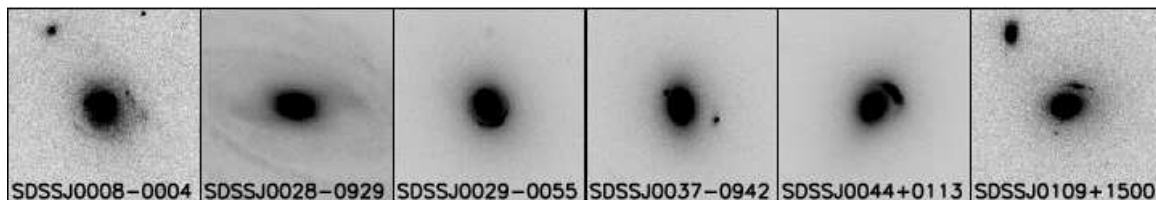


FIG. 5.— *HST*-ACS WFC imaging through the F814W filter of SLACS targets. Images are  $10'' \times 10''$ , with North up and East to the left. Cosmic-ray pixels in single-exposure images have been replaced with smoothed image values. Grayscale is linear from  $-0.25X$  (white) to  $X$  (black), where  $X$  is the 98th percentile flux level in the image. A version of this figure with all 131 target panels is available through the electronic edition of the *Astrophysical Journal*, or through the website of the first author.

TABLE 4  
SLACS HST-ACS TARGET OBSERVATIONAL DATA

RA/Dec (J2000)	Plate-MJD- FiberID	$z_{\text{FG}}$	$z_{\text{BG}}$	$I_{814}$ (obs.)	$I_{814}$ extin.	$L_{V555}$ ( $10^9 L_{\odot}$ )	$R_e$ ( $''$ )	$L_{e2}/L_{\text{deV}}$	$B/A$ (deV)	$PA$ ( $^{\circ}$ )	$\sigma_{\text{SDSS}}$ ( $\text{km s}^{-1}$ )	Classifi- cation
000802.96-000408.2	0669-52559-156	0.4400	1.1924	18.65d	0.12	86.7	1.71	0.313	0.83	27.3	...	E-S-A
002817.87-092934.3	0653-52145-590	0.0565	0.7146	13.75s	0.07	92.8	15.21	0.346	0.48	78.9	147±7	L-S-X
002907.77-005550.5	0391-51782-088	0.2270	0.9313	17.09d	0.04	76.3	2.16	0.310	0.84	26.6	229±18	E-S-A
003753.21-094220.1	0655-52162-392	0.1955	0.6322	16.26s	0.06	120.5	2.19	0.326	0.73	11.4	279±14	E-S-A
004402.90+011312.6	0393-51794-456	0.1196	0.1965	15.73s	0.04	68.8	2.61	0.321	0.76	151.3	266±13	E-S-A
010933.73+150032.5	0422-51811-508	0.2939	0.5248	17.75s	0.11	77.2	1.38	0.320	0.78	104.0	251±19	E-S-A
015758.94-005626.1	0700-52199-020	0.5132	0.9243	18.64d	0.05	117.3	1.06	0.310	0.69	69.2	...	E-S-A
021652.54-081345.3	0668-52162-428	0.3317	0.5235	16.93d	0.07	206.4	2.67	0.312	0.79	81.2	333±23	E-S-A
025245.21+003958.4	0807-52295-614	0.2803	0.9818	18.04d	0.15	55.8	1.39	0.317	0.94	97.2	164±12	E-S-A
033012.14-002051.9	0810-52672-252	0.3507	1.0709	18.16d	0.16	82.3	1.20	0.306	0.77	109.6	212±21	E-S-A
035458.47-064842.8	0464-51908-310	0.1301	0.3808	15.90s	0.14	76.9	3.76	0.316	0.88	9.1	160±8	E-S-X
040535.41-045552.4	0465-51910-406	0.0753	0.8098	16.45s	0.21	15.8	1.36	0.320	0.69	20.3	160±8	E-S-A
072804.95+383525.7	1733-53047-154	0.2058	0.6877	16.74d	0.12	91.2	1.78	0.316	0.74	67.0	214±11	E-S-A
073728.45+321618.6	0541-51959-145	0.3223	0.5812	17.04d	0.08	177.8	2.82	0.312	0.85	104.1	338±17	E-S-A
074251.84+345001.9	0542-51993-386	0.0853	0.7390	17.02s	0.11	11.0	1.77	0.314	0.97	124.5	165±10	E-S-X
075834.68+303443.3	1061-52641-256	0.1156	0.5013	16.05s	0.10	50.3	1.37	0.320	0.81	108.0	191±10	E-S-B
080240.82+450452.7	0436-51883-633	0.1423	0.4523	16.16s	0.09	70.3	2.71	0.315	0.80	86.0	244±12	E-S-X
080358.21+453655.6	0439-51877-333	0.1313	0.2938	16.90s	0.15	31.6	1.07	0.315	0.36	69.5	228±12	L-S-X
080858.78+470638.9	0438-51884-555	0.2195	1.0251	...	0.09	...	...	...	...	...	...	E-M-A*
081931.93+453444.8	0441-51868-108	0.1943	0.4462	17.07s	0.08	57.6	1.98	0.319	0.78	40.4	225±15	E-S-B
082242.32+265243.5	1267-52932-253	0.2414	0.5941	16.99d	0.05	95.4	1.82	0.312	0.74	87.0	259±15	E-S-A
084128.81+382413.7	0828-52317-012	0.1159	0.6567	15.34d	0.06	94.6	4.21	0.318	0.58	92.9	225±11	L-S-A
084706.89+031822.6	0564-52224-542	0.1192	0.4146	16.80s	0.05	25.7	1.91	0.320	0.69	120.1	199±12	E-S-X
090315.19+411609.1	1200-52668-398	0.4304	1.0645	17.95d	0.03	144.7	1.78	0.308	0.89	1.6	...	E-S-A
090319.52+313951.2	1590-52974-622	0.2711	0.5494	16.77d	0.04	150.0	3.03	0.319	0.67	147.8	258±15	E-S-B
091053.11+052023.2	1193-52652-232	0.2706	1.0741	...	0.08	...	...	...	...	...	...	E-M-B
091205.31+002901.2	0472-51955-429	0.1642	0.3239	15.57d	0.05	156.4	3.87	0.330	0.67	11.7	326±16	E-S-A
091244.31+413637.0	1200-52668-588	0.0646	0.1377	15.85s	0.04	17.3	1.24	0.337	0.65	22.7	218±11	E-S-X
092559.35+081411.8	1302-52763-012	0.1345	0.2251	17.66s	0.09	15.6	1.44	0.322	0.83	67.2	...	E-S-X
093425.13+603423.5	0486-51910-241	0.1011	0.2440	16.37s	0.06	27.5	1.65	0.313	0.56	48.4	208±10	E-S-X
093543.93-000334.8	0476-52314-177	0.3475	0.4670	16.75s	0.06	268.5	4.24	0.311	0.90	145.2	396±35	E-S-A
093600.77+091335.8	1303-53050-078	0.1897	0.5880	16.52d	0.07	90.5	2.11	0.308	0.81	145.3	243±12	E-S-A
094656.68+100652.8	1305-52757-503	0.2219	0.6085	17.09d	0.05	73.2	2.35	0.316	0.96	10.3	263±21	E-S-A
095320.42+520543.7	0902-52409-577	0.1315	0.4673	17.26s	0.01	20.1	1.22	0.319	0.88	45.5	229±19	E-S-X
095519.72+010144.4	0268-51633-336	0.1109	0.3159	16.97s	0.05	18.9	1.09	0.304	0.39	108.6	192±13	L-S-A
095629.78+510006.6	0902-52409-068	0.2405	0.4699	16.68d	0.02	122.7	2.19	0.311	0.73	147.7	334±17	E-S-A
095900.96+441639.4	0942-52703-499	0.2369	0.5315	16.90d	0.02	97.6	1.98	0.317	0.87	55.9	244±19	E-S-A
095944.07+041017.0	0572-52289-495	0.1260	0.5350	16.92d	0.05	25.9	1.39	0.298	0.60	58.4	197±13	E-S-A
101622.86+385903.3	1427-52996-461	0.1679	0.4394	16.71d	0.03	56.7	1.46	0.320	0.85	63.3	247±13	E-S-A
102026.54+112241.1	1598-53033-353	0.2822	0.5530	17.21d	0.06	110.5	1.59	0.319	0.79	106.6	282±18	E-S-A
102332.26+423001.8	1359-53002-418	0.1912	0.6960	16.77d	0.03	70.1	1.77	0.314	0.85	167.5	242±15	E-S-A
102551.32-003517.5	0272-51941-151	0.1589	0.2764	15.41s	0.12	181.2	4.94	0.312	0.76	112.3	264±13	E-S-X
102922.94+042001.8	0576-52325-433	0.1045	0.6154	16.13d	0.06	36.7	1.56	0.315	0.52	127.9	210±11	E-S-A
102927.53+611505.3	0772-52375-140	0.1574	0.2512	16.06s	0.02	88.8	2.73	0.360	0.83	3.1	228±14	E-S-B
103235.84+532234.9	0905-52643-100	0.1334	0.3290	17.05d	0.03	25.5	0.81	0.306	0.44	136.5	296±15	L-S-A
103904.22+051335.8	0577-52367-571	0.0668	0.3627	15.38s	0.05	28.7	2.40	0.323	0.87	59.0	190±10	E-S-X
103957.78+093351.0	1240-52734-507	0.2212	0.5612	...	0.05	...	...	...	...	...	...	E-M-B

NOTE. — Plate-MJD-Fiber constitute a unique SDSS spectrum identifier. Redshifts  $z_{\text{FG}}$  and  $z_{\text{BG}}$  are for foreground and background galaxies respectively, as measured from SDSS data:  $z_{\text{FG}}$  values are taken directly from the SDSS database, while  $z_{\text{BG}}$  values are measured as described in Bolton et al. (2004). Apparent magnitudes  $I_{814}$  are from *HST*-ACS de Vaucouleurs models, and are quoted in the AB system *without* correction for Galactic extinction. Magnitudes are measured from either 420-s Snapshot exposures (“s” for “snap”) or full-orbit multi-exposure images (“d” for “deep”). *I*-band Galactic dust extinction values based on Schlegel et al. (1998) maps are given separately, and should be subtracted from observed magnitudes to give dust-corrected magnitudes. Rest-frame luminosities  $L_{V555}$  are as computed from  $I_{814}$  with corrections for Galactic extinction, evolution, *k*-correction, and cosmological distance modulus as described in the text, assuming an absolute solar AB magnitude of  $V_{555, \odot} = 4.83$ . Effective radii  $R_e$  are measured from de Vaucouleurs image models, and quoted at the intermediate axis.  $L_{e2}/L_{\text{deV}}$  gives ratio of luminosity within  $R_e/2$  as determined from B-spline models to total de Vaucouleurs model luminosity.  $B/A$  gives ratio of minor to major axes for the de Vaucouleurs image models.  $PA$  gives de Vauc. major-axis position angles measured E from N. Velocity dispersions  $\sigma_{\text{SDSS}}$  are uncorrected for aperture effects. Reported errors are limited to a minimum of  $0.05\sigma_{\text{SDSS}}$ . No  $\sigma_{\text{SDSS}}$  values are reported for systems whose median SNR is less than 10 over the range of rest-frame wavelengths used for the fit, or for systems with multiple foreground galaxies. “Classification” column gives codes denoting (1) foreground-galaxy morphology, (2) foreground-galaxy multiplicity, and (3) status of system as a lens based on available data. Morphology is coded by “E” for early-type (elliptical and S0), “L” for late-type (Sa and later), and “U” for unclassified (galaxies that cannot be unambiguously classed as early- or late-type based on the *HST*-ACS data). Multiplicity is coded by “S” for single and “M” for multiple. Lens status is coded by “A” for systems with clear and convincing evidence of multiple imaging, “B” for systems with strong evidence of multiple imaging but insufficient SNR for definite conclusion and/or modeling, and “X” for all other systems (non-lenses and non-detections). Systems marked as “A\*” are definite lenses, but are not modeled for reasons specified in Table 6.

TABLE 4  
(CONTINUED)

RA/Dec (J2000)	Plate-MJD- FiberID	$z_{FG}$	$z_{BG}$	$I_{814}$ (obs.)	$I_{814}$ extin.	$L_{V555}$ ( $10^9 L_{\odot}$ )	$R_e$ (")	$L_{e2}/$ $L_{deV}$	$B/A$ (deV)	$PA$ ( $^{\circ}$ )	$\sigma_{SDSS}$ ( $\text{km s}^{-1}$ )	Classifi- cation
104606.93+415116.1	1361-53047-077	0.1025	0.7584	16.61d	0.02	22.0	1.03	0.308	0.36	49.8	191 $\pm$ 10	L-S-X
110024.39+532913.9	1011-52652-175	0.3171	0.8581	17.18s	0.02	143.6	2.24	0.314	0.58	103.0	...	E-S-A
110308.21+532228.2	1011-52652-156	0.1582	0.7353	16.43d	0.02	63.7	1.95	0.330	0.46	45.5	196 $\pm$ 12	U-S-A
110646.15+522837.8	1011-52652-007	0.0955	0.4069	15.52s	0.02	51.4	1.68	0.324	0.63	57.3	262 $\pm$ 13	E-S-A
110817.70+025241.3	0509-52374-471	0.1368	0.3105	17.19s	0.08	24.7	1.17	0.322	0.86	146.1	178 $\pm$ 14	E-S-B
111250.60+082610.4	1221-52751-028	0.2730	0.6295	17.22s	0.06	101.9	1.50	0.328	0.77	137.5	320 $\pm$ 20	E-S-A
111739.60+053414.0	0835-52326-571	0.2285	0.8230	17.11s	0.12	81.4	2.20	0.308	0.72	43.9	277 $\pm$ 19	E-S-B
113405.89+602713.5	0952-52409-524	0.1528	0.4742	16.44s	0.02	59.1	2.02	0.325	0.83	155.0	239 $\pm$ 12	E-S-A
113636.14+042625.0	0837-52642-039	0.1282	0.5341	16.97s	0.04	25.4	0.88	0.330	0.81	123.9	258 $\pm$ 14	E-S-X
114052.69+564044.5	1312-52781-311	0.0674	0.2968	15.78s	0.02	19.6	1.92	0.321	0.69	145.9	163 $\pm$ 9	L-S-X
114257.35+100111.8	1226-52734-306	0.2218	0.5039	17.10d	0.10	75.8	1.91	0.314	0.89	95.4	221 $\pm$ 22	E-S-A
114329.64-014430.0	0328-52282-535	0.1060	0.4019	14.96d	0.03	108.5	4.80	0.337	0.80	118.7	269 $\pm$ 13	E-S-A
115208.97+055431.0	0284-51943-452	0.1062	0.1590	16.90s	0.04	18.5	0.86	0.328	0.58	123.5	235 $\pm$ 14	E-S-X
115310.79+461205.3	1446-53080-211	0.1797	0.8751	17.20d	0.04	41.9	1.16	0.323	0.90	2.9	226 $\pm$ 15	E-S-A
115510.06+623722.4	0777-52320-501	0.3751	0.6690	17.61s	0.03	141.3	2.88	0.323	0.77	176.9	...	E-S-X
115905.46+544738.3	1018-52672-279	0.0818	0.2695	15.74d	0.02	30.6	1.90	0.318	0.69	107.3	231 $\pm$ 12	E-S-X
120324.89+023301.1	0517-52024-352	0.1644	0.4380	16.59s	0.05	61.2	2.70	0.312	0.50	67.2	209 $\pm$ 11	L-S-X
120444.07+035806.4	0842-52376-208	0.1644	0.6307	16.84s	0.04	48.1	1.47	0.316	0.97	132.1	267 $\pm$ 17	E-S-A
120540.44+491029.4	0969-52442-134	0.2150	0.4808	16.56d	0.04	110.4	2.59	0.314	0.72	158.3	281 $\pm$ 14	E-S-A
121158.75+455036.6	1370-53090-427	0.1110	0.3170	15.63d	0.02	63.6	2.89	0.322	0.75	107.6	231 $\pm$ 12	E-S-X
121340.58+670829.0	0493-51957-145	0.1229	0.6402	15.60d	0.03	81.1	3.23	0.326	0.77	20.0	292 $\pm$ 15	E-S-A
121826.70+083050.3	1625-53140-415	0.1350	0.7172	15.74d	0.03	87.2	3.18	0.321	0.72	50.5	219 $\pm$ 11	E-S-A
124426.03+011146.8	0291-51928-528	0.0725	0.5600	15.21s	0.03	39.2	2.83	0.320	0.70	106.9	172 $\pm$ 9	L-S-X
125028.26+052349.1	0847-52426-549	0.2318	0.7953	16.70d	0.05	115.4	1.81	0.310	0.97	114.8	252 $\pm$ 14	E-S-A
125050.52-013531.7	0337-51997-460	0.0871	0.3526	15.14s	0.04	61.7	2.93	0.317	0.72	125.3	246 $\pm$ 12	U-S-A*
125135.71-020805.2	0337-51997-480	0.2243	0.7843	17.25s	0.04	63.8	2.61	0.299	0.51	39.5	...	L-S-A
125919.05+613408.6	0783-52325-279	0.2334	0.4488	16.85s	0.02	98.9	1.81	0.314	0.79	96.1	253 $\pm$ 16	E-S-A*
131326.70+050657.2	0851-52376-344	0.1438	0.3385	17.10s	0.06	29.4	0.86	0.311	0.45	74.9	221 $\pm$ 17	L-S-B
133045.53-014841.6	0910-52377-503	0.0808	0.7115	16.99s	0.07	9.8	0.89	0.315	0.46	103.6	185 $\pm$ 9	E-S-B
134308.25+602755.0	0786-52319-236	0.1198	0.3199	16.30s	0.03	40.6	2.07	0.310	0.52	153.1	178 $\pm$ 10	L-S-X
134309.22+605209.7	0786-52319-193	0.0343	0.0880	13.64s	0.03	35.8	4.91	0.322	0.49	5.1	206 $\pm$ 10	E-S-X
140228.21+632133.5	0605-52353-503	0.2046	0.4814	16.33d	0.03	122.1	2.70	0.316	0.77	70.8	267 $\pm$ 17	E-S-A
140329.49+000641.4	0302-51688-354	0.1888	0.4730	17.11s	0.08	52.8	1.46	0.317	0.81	110.5	213 $\pm$ 17	E-S-A
141622.34+513630.4	1045-52725-464	0.2987	0.8111	17.57d	0.02	87.5	1.43	0.326	0.76	23.4	240 $\pm$ 25	E-S-A
142015.85+601914.8	0788-52338-605	0.0629	0.5351	15.08d	0.03	32.8	2.06	0.326	0.57	111.5	205 $\pm$ 10	E-S-A
143004.10+410557.1	1349-52797-406	0.2850	0.5753	16.87d	0.02	149.4	2.55	0.309	0.79	120.7	322 $\pm$ 32	E-S-A
143039.86+511530.9	1046-52460-448	0.1337	0.4503	16.33s	0.02	48.9	1.81	0.333	0.68	74.1	206 $\pm$ 10	L-S-X
143213.34+631703.8	0499-51988-005	0.1230	0.6643	15.16d	0.03	122.5	5.85	0.307	0.96	107.2	199 $\pm$ 10	L-S-A
143609.50+493927.3	1046-52460-025	0.1225	0.3145	16.32s	0.04	42.4	2.13	0.312	0.71	12.9	212 $\pm$ 12	E-S-X
143627.54-000029.2	0306-51637-035	0.2852	0.8049	17.24s	0.07	112.2	2.24	0.315	0.75	151.3	224 $\pm$ 17	E-S-A
144319.62+030408.2	0587-52026-205	0.1338	0.4187	17.06s	0.06	26.1	0.94	0.320	0.62	61.1	209 $\pm$ 11	E-S-A
144858.24-011614.6	0920-52411-607	0.1474	0.7807	16.65s	0.10	48.2	1.39	0.302	0.41	34.4	187 $\pm$ 10	L-S-X
145128.19-023936.4	0921-52380-293	0.1254	0.5203	16.09d	0.16	61.0	2.48	0.315	0.98	40.6	223 $\pm$ 14	E-S-A
145218.94-005820.2	0309-51994-298	0.1770	0.5131	17.28s	0.08	39.3	0.85	0.321	0.77	120.9	193 $\pm$ 11	E-S-X
151505.14+612848.3	0611-52055-626	0.2421	0.3800	17.31s	0.03	70.3	1.20	0.327	0.66	173.0	212 $\pm$ 25	E-S-X
152009.08-003457.3	0313-51673-306	0.1140	0.3954	16.88s	0.11	23.0	1.61	0.324	0.59	30.7	196 $\pm$ 16	L-S-X
152444.37-005209.1	0924-52409-527	0.1524	0.7323	17.39s	0.28	31.0	1.62	0.313	0.82	54.8	150 $\pm$ 22	E-S-X
152506.70+332747.4	1387-53118-532	0.3583	0.7173	17.11d	0.04	204.0	2.90	0.316	0.61	135.4	264 $\pm$ 26	E-S-A
152524.63+011401.7	0313-51673-523	0.1294	0.6269	16.68s	0.09	35.3	1.59	0.319	0.85	58.1	158 $\pm$ 10	E-S-X
153150.07-010545.7	0314-51641-124	0.1596	0.7439	16.08s	0.26	112.6	2.50	0.320	0.68	143.5	279 $\pm$ 14	E-S-A
153530.38-003852.3	0315-51663-259	0.1613	0.6585	16.81s	0.21	55.9	1.23	0.325	0.60	98.2	254 $\pm$ 15	E-S-X
153711.26+412554.6	1679-53149-628	0.1423	0.6811	17.02d	0.04	30.3	2.07	0.316	0.84	1.7	204 $\pm$ 14	E-S-X
153812.92+581709.8	0615-52347-594	0.1428	0.5312	16.66s	0.03	42.0	1.58	0.311	0.82	153.5	189 $\pm$ 12	E-S-A
154100.77+413058.7	1053-52468-275	0.1423	0.5033	16.84d	0.05	36.2	1.15	0.320	0.42	64.0	215 $\pm$ 11	L-S-X
154731.22+572000.0	0617-52072-561	0.1883	0.3958	16.25s	0.02	109.4	2.53	0.317	0.89	156.8	254 $\pm$ 13	E-S-X
155003.12+525846.7	0618-52049-458	0.0491	0.7396	15.23s	0.03	17.1	2.04	0.335	0.75	108.9	202 $\pm$ 10	E-S-B
160453.49+335546.2	1418-53142-599	0.0786	0.3500	15.36d	0.05	40.7	2.59	0.319	0.63	97.2	228 $\pm$ 11	E-S-B
161437.74+452253.3	0814-52443-510	0.1779	0.8113	16.83s	0.02	56.9	2.58	0.316	0.90	60.5	182 $\pm$ 13	E-S-B
161843.10+435327.4	0815-52374-337	0.1989	0.6657	...	0.03	...	...	...	...	...	...	E-M-A*
162132.99+393144.6	1172-52759-318	0.2449	0.6021	16.81s	0.01	113.2	2.14	0.312	0.73	142.9	236 $\pm$ 20	E-S-A
162746.45-005357.6	0364-52000-084	0.2076	0.5241	16.91d	0.18	85.1	1.98	0.312	0.85	6.9	290 $\pm$ 15	E-S-A
163028.16+452036.3	0626-52057-518	0.2479	0.7933	16.79d	0.01	118.4	1.96	0.318	0.84	71.7	276 $\pm$ 16	E-S-A

TABLE 4  
(CONTINUED)

RA/Dec (J2000)	Plate-MJD- FiberID	$z_{\text{FG}}$	$z_{\text{BG}}$	$I_{814}$ (obs.)	$I_{814}$ extin.	$L_{V555}$ ( $10^9 L_{\odot}$ )	$R_e$ (")	$L_{e2}/$ $L_{\text{deV}}$	$B/A$ (deV)	$PA$ ( $^{\circ}$ )	$\sigma_{\text{SDSS}}$ ( $\text{km s}^{-1}$ )	Classifi- cation
163339.26−001256.2	0348-51671-234	0.0702	0.2060	15.81s	0.17	23.9	2.28	0.323	0.52	169.7	215±11	U-S-X
163602.62+470729.6	0627-52144-464	0.2282	0.6745	17.03s	0.04	81.5	1.68	0.321	0.78	102.2	231±15	E-S-A
170013.98+622109.7	0349-51699-043	0.1228	0.3584	16.52s	0.05	35.3	1.53	0.314	0.72	118.5	192±10	E-S-X
170216.76+332044.8	0973-52426-464	0.1785	0.4357	16.10s	0.04	113.2	3.66	0.313	0.78	116.3	256±14	E-S-B
170603.69+330400.9	0974-52427-127	0.1682	0.7736	16.85d	0.04	50.5	1.38	0.321	0.79	26.3	225±12	E-S-B
171723.13+573948.2	0355-51788-542	0.1144	0.5748	16.02s	0.06	48.9	2.08	0.315	0.77	145.6	227±11	E-S-X
171837.40+642452.2	0352-51789-563	0.0899	0.7366	...	0.06	...	...	...	...	...	...	E-M-A*
211112.27−003826.5	0986-52443-256	0.1933	0.4761	...	0.15	...	...	...	...	...	...	E-M-B
211949.65−074201.7	0639-52146-142	0.1704	0.5262	16.76s	0.40	78.0	1.91	0.311	0.64	139.4	207±17	E-S-B
212151.12+120312.9	0730-52466-327	0.1434	0.4862	16.92s	0.12	36.3	1.61	0.313	0.59	66.9	194±12	L-S-B
214154.68−000112.3	0989-52468-035	0.1380	0.7127	16.83s	0.10	35.8	1.81	0.300	0.37	88.4	181±14	L-S-A*
220218.32−084648.0	0717-52468-165	0.1613	0.5011	17.13s	0.07	36.6	1.13	0.312	0.34	12.7	231±12	L-S-X
220956.93−075447.9	0718-52206-475	0.1112	0.2148	17.58s	0.09	11.2	0.71	0.317	0.49	178.3	229±16	E-S-X
222537.34+125957.6	0737-52518-119	0.3103	0.6571	18.09d	0.15	66.2	0.74	0.325	0.75	136.7	248±24	E-S-X
223840.20−075456.0	0722-52224-442	0.1371	0.7126	16.20d	0.07	61.2	2.33	0.315	0.74	138.3	198±11	E-S-A
224155.71+122814.0	0739-52520-054	0.0998	0.7173	15.92s	0.07	40.9	4.55	0.350	0.54	164.8	176±13	L-S-X
230053.15+002238.0	0677-52606-520	0.2285	0.4635	17.07d	0.10	83.1	1.83	0.321	0.80	85.7	279±17	E-S-A
230220.18−084049.5	0725-52258-463	0.0901	0.2224	15.53s	0.07	47.4	2.25	0.325	0.80	169.1	237±12	E-S-A*
230321.72+142217.9	0743-52262-304	0.1553	0.5170	16.10d	0.35	112.9	3.28	0.321	0.64	36.7	255±16	E-S-A
232120.93−093910.3	0645-52203-517	0.0819	0.5324	14.66s	0.05	84.6	4.11	0.313	0.78	127.9	249±12	E-S-A
234111.57+000018.7	0682-52525-594	0.1860	0.8070	16.36d	0.05	98.7	3.15	0.318	0.59	78.8	207±13	E-S-A
234728.08−000521.3	0684-52523-311	0.4169	0.7145	17.89s	0.06	145.3	1.40	0.309	0.71	16.5	...	E-S-B

TABLE 5  
SLACS HST-ACS GRADE-A STRONG LENS MODEL PARAMETERS

System Name (SDSS...)	$b_{\text{SIE}}$ (")	$q$ (SIE)	$PA$ (SIE)	$L_{\text{Ein,SIE}}/$ $L_{\text{deV}}$	$b_{\text{LTM}}$ (")	$\gamma_{\text{ext}}$ (LTM)	$PA_{\gamma}$ (LTM)	$L_{\text{Ein,LTM}}/$ $L_{\text{deV}}$	$N_{\text{src}}$	Ring Subset?	Good $\sigma_{\text{SDSS}}?$
J0008−0004	1.16	0.70	35.2	0.393	1.14	0.09	37.6	0.387	3	No	No
J0029−0055	0.96	0.89	25.4	0.284	0.95	0.01	33.1	0.282	2	Yes	Yes
J0037−0942	1.53	0.84	15.9	0.404	1.52	0.01	67.1	0.401	2	No	Yes
J0044+0113	0.79	0.66	7.4	0.218	0.76	0.12	19.4	0.211	2	No	Yes
J0109+1500	0.69	0.55	99.8	0.321	0.68	0.07	83.8	0.317	1	No	Yes
J0157−0056	0.79	0.72	102.6	0.401	0.67	0.24	103.1	0.362	3	No	No
J0216−0813	1.16	0.79	73.3	0.283	1.15	0.03	78.6	0.282	3	No	Yes
J0252+0039	1.04	0.93	106.2	0.441	1.03	0.01	99.2	0.439	3	Yes	Yes
J0330−0020	1.10	0.81	113.2	0.459	1.04	0.07	113.9	0.443	3	No	Yes
J0405−0455	0.80	0.72	21.0	0.355	0.79	0.05	23.5	0.354	1	Yes	Yes
J0728+3835	1.25	0.85	67.6	0.392	1.25	0.01	170.6	0.393	4	Yes	Yes
J0737+3216	1.00	0.67	98.8	0.239	0.97	0.10	97.8	0.233	2	Yes	Yes
J0822+2652	1.17	0.88	68.2	0.370	1.14	0.01	10.5	0.365	2	Yes	Yes
J0841+3824	1.41	0.79	91.4	0.242	1.36	0.05	10.2	0.236	2	No	Yes
J0903+4116	1.29	0.90	161.3	0.396	1.27	0.02	142.4	0.393	2	Yes	No
J0912+0029	1.63	0.56	8.2	0.288	1.62	0.10	5.1	0.286	1	Yes	Yes
J0935−0003	0.87	0.69	22.2	0.160	0.81	0.13	27.0	0.152	1	No	Yes
J0936+0913	1.09	0.89	160.1	0.315	1.09	0.02	16.7	0.315	2	Yes	Yes
J0946+1006	1.38	0.81	159.2	0.355	1.39	0.08	157.9	0.357	2	Yes	Yes
J0955+0101	0.91	0.82	62.5	0.458	1.03	0.27	27.6	0.499	2	No	Yes
J0956+5100	1.33	0.63	146.2	0.356	1.30	0.11	144.2	0.351	1	Yes	Yes
J0959+4416	0.96	0.92	57.4	0.310	0.96	0.00	35.0	0.310	2	No	Yes
J0959+0410	0.99	0.86	66.9	0.397	1.01	0.07	142.1	0.402	2	No	Yes
J1016+3859	1.09	0.78	46.4	0.414	1.06	0.08	38.9	0.406	2	No	Yes
J1020+1122	1.20	0.80	135.8	0.413	1.21	0.10	152.6	0.416	2	No	Yes
J1023+4230	1.41	0.87	170.4	0.435	1.40	0.03	168.8	0.433	3	Yes	Yes
J1029+0420	1.01	0.84	93.9	0.378	1.10	0.17	48.0	0.401	1	No	Yes

NOTE. — Einstein radii  $b_{\text{SIE}}$  and  $b_{\text{LTM}}$  are quoted for an intermediate-axis normalization. Mass minor-to-major axis ratios of SIE models are given by  $q_{\text{SIE}}$ . External shear values for LTM models are given by  $\gamma_{\text{ext}}$ . Position angles  $PA$  (of SIE major axis) and  $PA_{\gamma}$  (of LTM external shear) are measured in degrees E of N.  $L_{\text{Ein,SIE}}/L_{\text{deV}}$  and  $L_{\text{Ein,LTM}}/L_{\text{deV}}$  give luminosity enclosed within SIE and LTM Einstein radii, evaluated using B-spline luminosity models, as a fraction of de Vaucouleurs total model luminosity.  $N_{\text{src}}$  gives number of source-plane components used to model background galaxy. “Ring Subset?” column indicates whether lens is included in the subset of systems with full or partial Einstein-ring lensed images. “Good  $\sigma_{\text{SDSS}}?$ ” column indicates whether velocity dispersion is well-measured in SDSS data.



TABLE 5  
(CONTINUED)

System Name (SDSS...)	$b_{\text{SIE}}$ ( $''$ )	$q$ (SIE)	$PA$ (SIE)	$L_{\text{Ein,SIE}}$ $/L_{\text{deV}}$	$b_{\text{LTM}}$ ( $''$ )	$\gamma_{\text{ext}}$ (LTM)	$PA_{\gamma}$ (LTM)	$L_{\text{Ein,LTM}}$ $/L_{\text{deV}}$	$N_{\text{src}}$	Ring Subset?	Good $\sigma_{\text{SDSS}}?$
J1032+5322	1.03	0.76	139.7	0.582	1.12	0.08	46.2	0.606	3	No	Yes
J1100+5329	1.52	0.53	105.3	0.384	1.43	0.19	113.4	0.369	2	No	No
J1103+5322	1.02	0.52	51.7	0.342	1.04	0.05	71.9	0.348	1	Yes	Yes
J1106+5228	1.23	0.76	56.3	0.407	1.23	0.02	52.3	0.406	1	Yes	Yes
J1112+0826	1.49	0.75	146.5	0.503	1.37	0.03	166.7	0.482	2	No	Yes
J1134+6027	1.10	0.77	102.1	0.343	0.88	0.23	90.2	0.298	1	No	Yes
J1142+1001	0.98	0.83	99.5	0.320	0.92	0.06	89.8	0.307	1	No	Yes
J1143-0144	1.68	0.75	120.1	0.267	1.66	0.04	119.4	0.265	3	No	Yes
J1153+4612	1.05	0.77	21.6	0.460	1.05	0.09	31.1	0.462	1	Yes	Yes
J1204+0358	1.31	0.84	65.4	0.455	1.27	0.08	64.6	0.446	2	Yes	Yes
J1205+4910	1.22	0.70	156.6	0.302	1.20	0.06	158.3	0.299	1	Yes	Yes
J1213+6708	1.42	0.83	14.5	0.297	1.38	0.02	164.6	0.292	1	No	Yes
J1218+0830	1.45	0.75	51.5	0.300	1.44	0.03	54.9	0.299	1	No	Yes
J1250+0523	1.13	0.96	130.8	0.366	1.11	0.01	140.5	0.362	5	Yes	Yes
J1251-0208	0.84	0.67	33.9	0.218	0.85	0.07	156.5	0.221	2	No	No
J1402+6321	1.35	0.83	64.4	0.316	1.36	0.02	34.4	0.317	2	Yes	Yes
J1403+0006	0.83	0.81	140.8	0.354	0.83	0.05	169.4	0.354	4	Yes	Yes
J1416+5136	1.37	0.94	71.4	0.483	1.36	0.04	96.7	0.482	3	No	Yes
J1420+6019	1.04	0.67	111.3	0.329	1.07	0.01	108.7	0.335	2	Yes	Yes
J1430+4105	1.52	0.68	111.7	0.355	1.46	0.10	110.3	0.344	6	Yes	Yes
J1432+6317	1.26	0.96	130.4	0.153	1.25	0.01	152.0	0.151	2	No	Yes
J1436-0000	1.12	0.72	156.2	0.315	1.08	0.07	162.6	0.308	1	No	Yes
J1443+0304	0.81	0.73	78.1	0.438	0.78	0.08	97.9	0.427	1	No	Yes
J1451-0239	1.04	0.97	106.3	0.277	1.03	0.02	113.8	0.274	1	No	Yes
J1525+3327	1.31	0.51	134.3	0.292	1.30	0.11	132.5	0.291	1	No	Yes
J1531-0105	1.71	0.77	142.9	0.393	1.71	0.03	139.4	0.393	2	Yes	Yes
J1538+5817	1.00	0.89	152.1	0.365	0.99	0.01	146.6	0.363	2	Yes	Yes
J1621+3931	1.29	0.77	148.7	0.358	1.29	0.03	161.9	0.358	1	No	Yes
J1627-0053	1.23	0.91	10.5	0.360	1.22	0.00	60.6	0.359	1	Yes	Yes
J1630+4520	1.78	0.87	74.9	0.475	1.78	0.02	84.1	0.475	4	Yes	Yes
J1636+4707	1.09	0.79	98.2	0.380	1.08	0.04	91.9	0.380	2	Yes	Yes
J2238-0754	1.27	0.85	137.4	0.335	1.28	0.00	72.2	0.335	2	Yes	Yes
J2300+0022	1.24	0.71	87.8	0.391	1.21	0.08	90.0	0.386	1	Yes	Yes
J2303+1422	1.62	0.61	35.3	0.318	1.60	0.07	33.8	0.316	2	Yes	Yes
J2321-0939	1.60	0.86	135.2	0.258	1.60	0.01	172.6	0.258	2	Yes	Yes
J2341+0000	1.44	0.76	96.6	0.295	1.47	0.07	143.3	0.299	4	Yes	Yes

TABLE 6  
SUMMARY OF UNMODELED GRADE-A LENSES

System Name	Comments
SDSSJ0808+4706	Nearby companion prevents simple SIE modeling.
SDSSJ1250-0135	Complicated by spiral structure and asymmetric bulge in foreground galaxy.
SDSSJ1259+6134	Faint <i>HST</i> and IFU features consistent with lensing; difficult to reconcile F814W and F435W images.
SDSSJ1618+4353	Double foreground galaxy.
SDSSJ1718+6424	Double foreground galaxy.
SDSSJ2141-0001	Spiral/dust structure in foreground galaxy prevents acceptable model subtraction.
SDSSJ2302-0840	Clear lens in IFU data; <i>HST</i> imaging inconclusive.

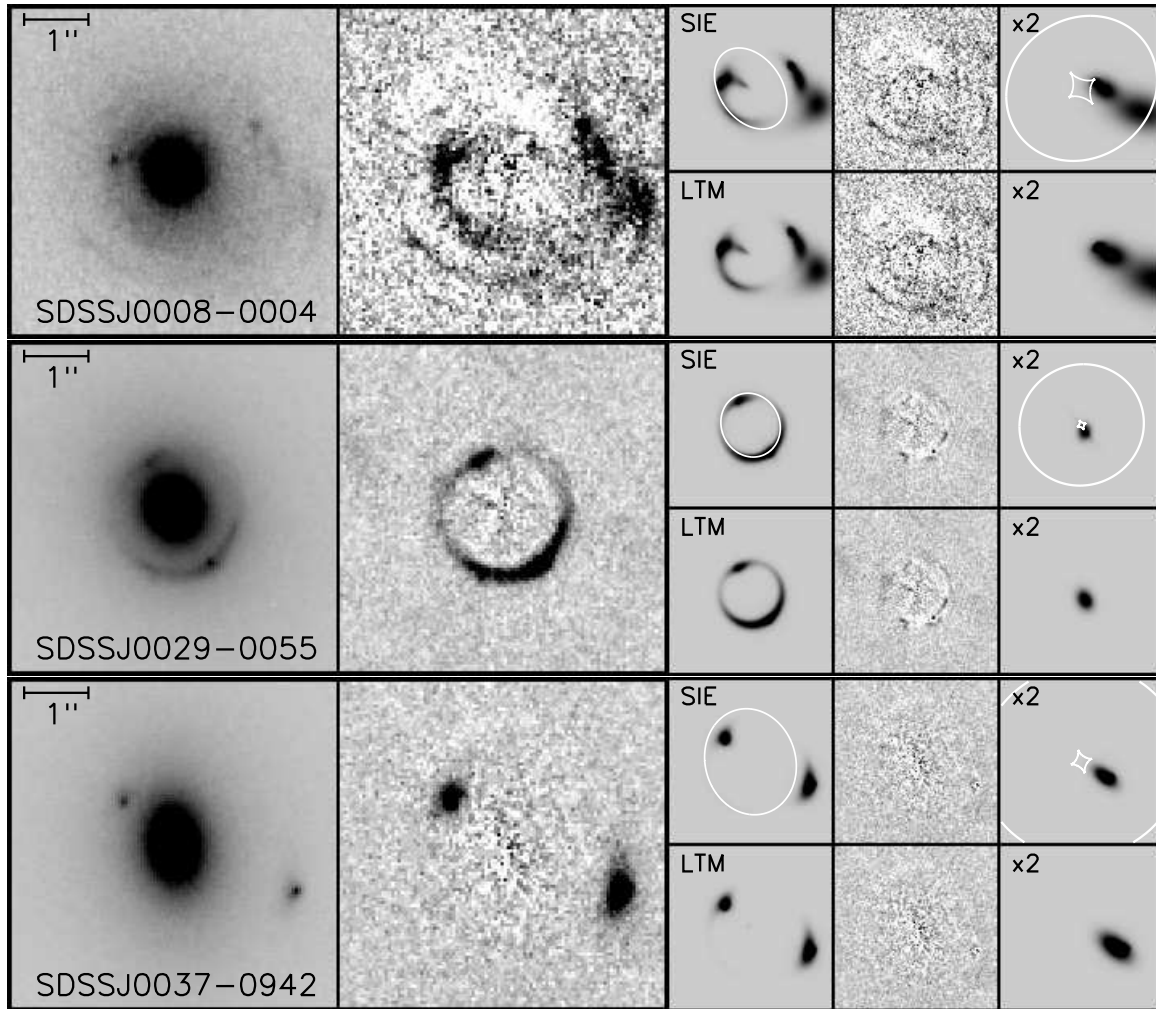


FIG. 6.— Lens models for grade-A SLACS *HST*-ACS strong gravitational lens systems. Leftmost large panels show direct F814W images,  $5'' \times 5''$  to a side, with North up and East left. Next large panels show same images, with B-spline model of foreground galaxy subtracted, showing lensed features. *Top rows of smaller panels:* Left: model prediction of best-fit SIE strong lens model for features in residual data image, with critical curve in white; Center: “double-residual” image, after subtraction of B-spline and SIE models; Right: un-lensed source-plane for best-fit SIE lens model, evaluated over a  $2.5'' \times 2.5''$  region and convolved with a  $2\times$  de-magnified *HST* PSF for display purposes, with caustics shown in white. *Bottom rows of smaller panels:* Same as top row, but for best-fit light-traces-mass (LTM) lens models and without critical curves or caustics. Grayscale is linear in all images, ranging from  $-0.25X$  (white) to  $X$  (black). For the direct images,  $X$  is set to the 97th-percentile image value as determined from the smooth B-spline model. For the residual and lens-model images,  $X$  is set to the 99th-percentile image value as determined from the SIE lens-model image. Figures for all 63 lens models are available through the electronic version of the *Astrophysical Journal*, or through the website of the first author.